Dislocations pinning by substitutional impurities in an atomic-scale model for the Al(Mg) solid solutions

Sylvain Patinet, Laurent Proville

Dislocations pinning by substitutional impurities in an atomic-scale model for the Al(Mg) solid solutions

Journal:	*Philosophical Magazine & Philosophical Magazine Letters*
Manuscript ID:	TPHM-10-Jun-0287.R2
Journal Selection:	Philosophical Magazine
Date Submitted by the Author:	19-Nov-2010
Complete List of Authors:	Patinet, Sylvain; CNRS/PMMH Proville, Laurent; CEA, DEN
Keywords:	aluminium alloys, dislocations, atomistic simulation, hardness
Keywords (user supplied):	

Philosophical Magazine
Vol. 00, No. 00, 00 Month 200x, 1–19

RESEARCH ARTICLE

Dislocations pinning by substitutional impurities in an atomic-scale model for the Al(Mg) solid solutions

S. Patinet* and L. Proville

CEA, DEN, Service de Recherches de Métallurgie Physique, F-91191 Gif-sur-Yvette, France

(*v1.1 released February 2009*)

We report our atomic-scale computations for the static depinning threshold of dislocations in the Al(Mg) solid solutions. The interaction between the dislocations and the isolated obstacles is studied for different types of obstacle, i.e., the single solute atoms situated at different positions and the solute dimers with different bond directions. A part of this work is used to apply different standard analytical theories for solid solution hardening, the predictions of which are finally compared with our direct atomic-scale simulations (AS) for the dislocation depinning in the random Al(Mg) solid solutions. According to our comparisons, the dislocation statistics in our AS is qualitatively well described by the Mott-Nabarro-Labusch theory. In agreement with earlier results about a different system, namely Ni(Al), the depinning thresholds are similar for the edge and for the screw dislocations.

1. Introduction

The origin of the macroscopic yield stress in metals is mainly ascribed to the pinning of dislocations by other extended defects as dislocations and grain boundaries and other point-like defects. Substitutional alloying elements are among such defects and lead to the well-known phenomenon of solid solution hardening (SSH). Avoiding the introduction of large inhomogeneities and thence material embrittlement, SSH is a standard process of metallurgy which, in spite of its relative importance in commercial alloy design and a number of experimental studies [1], is still difficult to predict accurately. One of the main challenges of the theory is to predict quantitatively the critical resolved shear stress (CRSS) as a function of the nature and the concentration of impurities. To take up this challenge, it is necessary to determine the relevant parameters associated with the SSH and to understand the role played by the different types of glissile dislocation.

The statistics of a dislocation impinging on a random distribution of obstacles was shown to depend on the details of the dislocation-obstacle interaction [2–9]. A dislocation gliding in a solid solution experiences both long-range and short-range interactions. The former stems from the Coulomb type stress field of the dislocation meanwhile the latter results from the dislocation core crossing with solute atoms situated in the vicinity of the glide plane. Although, the long range interaction can be described remarkably well through the linear elastic theory [10, 11], nearby the dislocation core such a linear theory is not applicable because of nonlinearity of the atomic interactions. The problem of the short range interaction can however

*Corresponding author. Email: sylvain.patinet@espci.fr Present address: Physique et Mécanique des Milieux Hétérogènes UMR 7636 du CNRS/ESPCI/Paris 6/Paris 7, 10, rue Vauquelin, 75231 Paris Cedex 5, France

ISSN: 1478-6435 print/ISSN 1478-6443 online

DOI: 10.1080/14786435.20xx.xxxxxx
http://www.informaworld.com

be addressed using three-dimensional atomic-scale simulations (AS) based on the Embedded Atom Method (EAM) [12–17]. Recently [18], the use of EAM allowed us to examine the dislocation pinning in a model Ni(Al) solid solution as a function of the dislocation character. Hereby we extend our study to another face centered cubic (fcc) alloy, namely Al(Mg) for which the EAM [19] model has been employed in several atomistic studies bearing on dislocation-solute interactions [20–23]. Interestingly, the system Al(Mg) contrasts with Ni(Al) on several physical features related to SSH theory, e.g., the size and modulus misfit of Mg atoms in Al, the stacking fault energy and the order energy of the alloy. Thence it is possible to verify whether the conclusions to which we came in Ni(Al) can be extended to another fcc solid solution. In the present work we examine the behaviour of the two glissile dislocation types, i.e., edge and screw in fcc crystals and we address the reliability of different SSH statistical models.

Our study is divided within two steps. The AS are used primarily to examine different features of the dislocation cores in the EAM model for pure Al. We determine the dissociation width, the Shockley partials core spreading and the Peierls stress. Such quantities are compared with their conventional estimates from the standard theory of dislocations [24]. The stiffness of the dislocations is then calculated from AS in order to derive the effective line tension of the different types of dislocation. The maximum pinning forces and the interaction ranges are computed for different obstacle configurations such as the isolated Mg solute atoms and the solute dimers. In the second step of our study, the static AS allow us to compute the CRSS for an isolated dislocation in a fully random solid solution as a function of the Mg content, c_{Mg} with 2 at. % $< c_{\mathrm{Mg}} <$ 10 at. %. The main results of the present work are : (i) the elementary interactions between the dislocations and the obstacles are found to be of the same order for the edge and the screw dislocations; (ii) in agreement with (i), the flow stress increase with Mg concentration is of same order for the edge and for the screw dislocation segments; (iii) the CRSS is found to follow a fractional power law of the solute concentration c_{Mg} close from the Mott-Nabarro-Labusch theory.

The paper is organized as follows. In Sec. 2, the atomic-scale method and the geometry of the simulation cell are described. The dislocation core geometry, the Peierls stress and the line tension are computed for the edge and for the screw dislocations in a pure Al crystal. In Sec. 3, we analyze the interaction between the dislocations and the different pinning configurations of Mg solutes. In Sec. 4, the prediction from the SSH analytical models are discussed in regard of our direct AS computations for the dislocation depinning threshold. In Sec. 5, the results are resumed.

2. Atomic-scale model for dislocations

2.1. *Simulation technics*

The inter-atomic potentials for Al(Mg) were derived in different studies [19, 25, 26]. In the context of the present work, it may be noted that this potential was derived from adjustment on electronic structure calculations (which is expected to provide some portability) and on experimental results. Originally, Liu et al. have built this potential to study the anisotropic surface segregation of Mg atoms for alloy concentration running from 1 to 10 at. %. The calculated dependence of the lattice parameter as a function of the solute concentration is close to the experiment value [27]. However, it does not correctly describes the variation of elastic moduli with Mg concentration. In particular, we found that the decrease of the C_{44} elastic

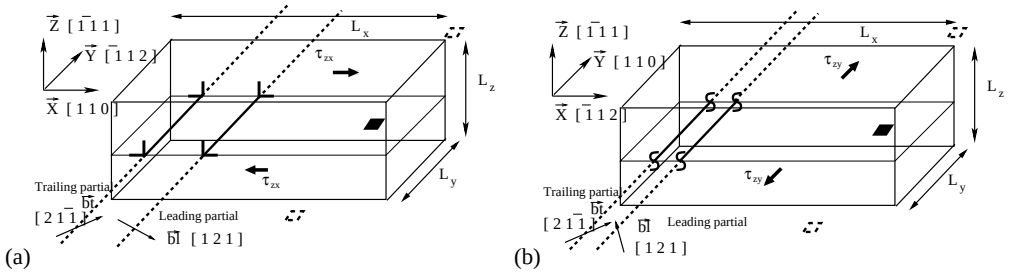

Figure 1. Schematic view of the simulation cell with a dissociated edge dislocation (a) and a screw one (b). The dislocations interact with Mg obstacles (squares) forming with the periodic images a regularly spaced chain of obstacles.

constant is overestimated compared to experiments [28] that are confirmed by electronic structure calculations [29]. The molecular dynamics code used in our study was developed in the *Service de Recherches de Métallurgie Physique laboratory. It was implemented originally by N. V. Doan [30], then adapted to the problematic of dislocation by D. Rodney [31] and used specifically in the context of solid solution hardening by E. Rodary [13] and L. Proville [32]. The current version of the code is named ADD, standing for Atomic Dislocation Dynamics.* The AS cell required to introduce a dislocation in a nano-crystal has been adapted from the slab geometry introduced by Rodney and Martin [31] and Osetsky and Bacon [33]. The dislocations glide through the crystal with 2 free surfaces parallel to the glide plane $(1\bar{1}1)$ (see Fig. 1). The edge and screw dislocations have a $b = 1/2[110]$ Burgers vector and are aligned with the $[\bar{1}12]$ and [110] direction, respectively. Periodic boundary conditions (PBC) are imposed in the dislocation line, denoted as Y, and in the glide direction, denoted as X. The Z direction is perpendicular to the glide plane. The atoms that compose the upper and lower free surfaces of the slab are constrained to a two-dimensional (2D) dynamics with a frozen motion in the Z direction. The external shear stress, τ_{xz} (τ_{yz}) for the edge (screw) dislocation is applied through additional constant forces on the frozen atoms. Between the constrained free surfaces, the cell height is $L_z = 15$ b. The length along X is $L_x = 40$ b and 70 b, for edge and screw dislocation, respectively. The cell length along the Y-axis, denoted by L_y, will take different values depending on which dislocation length has to be simulated. Three different types of simulations will be realized: (i) in the rest of Sec. 2 the simulation cell is made of a pure Al nano-crystal and the dislocation remains straight; (ii) in Sec. 3 the simulation cell contains an obstacle either made of an isolated Mg or a dimer with different configurations. In the latter case, the PBC along Y forms a regular array of obstacles with a separation distance between nearest obstacles which equals L_y. Varying L_y will allow us to modify the critical stress required to liberate the dislocation and thence to characterize the pinning force of each type of obstacle. The dislocation can then form some bows; (iii) in Sec. 4 the simulation cell is made of an Al(Mg) fully random solid solution. The Mg solute concentrations are imposed between $c_{Mg} = 2$ at. % and 10 at. %. In order to capture the statistics of a dislocation impinging on a random distribution of obstacles, the length along Y is chosen larger than the Larkin length[34], i.e., $L_y = 520$ b and 300 b, for the edge and for the screw dislocations, respectively. In each case, an over-damped noiseless Langevin dynamics is used to minimize the total simulation cell enthalpy.[18]

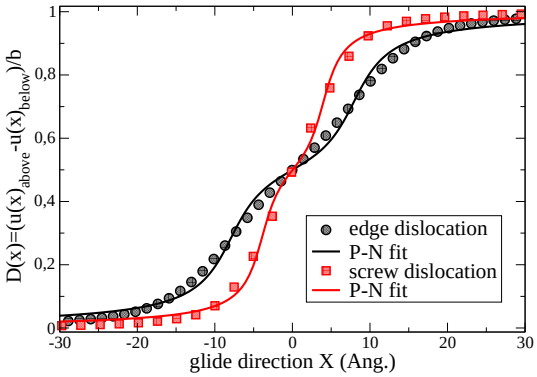

Figure 2. Normalized disregistry function D (see text) for the dislocation cores projected on the slip plane in the glide direction, X, for an edge (circle) and a screw (square) dislocation. The symbols correspond to atomic calculations while the lines are the results of the adjustment of the Peierls-Nabarro equation 1.

2.2. *Dislocation core*

The dislocation core features are first studied in a pure crystal of Al. After minimizing the total energy of the simulation cell, i.e., with no applied stress, the dislocation is straight and it dissociates into two Shockley partial dislocations, separated by a stacking fault region, as it is expected in fcc metals [35, 36]. For the slip system studied here, it is also expected that the Peierls potential is rather flat and the core of each partial spread over few atomic spacing. The Peierls-Nabarro (PN) model [24, 37, 38] provides thus a convenient way to parameterize the dislocation geometry. From AS, the dislocation displacement field is computed through the so-called disregistry function, i.e., the displacement difference $D(x) = u_{above}(x) - u_{below}(x)$ along the glide direction across the $(1\bar{1}1)$ slip plane. The displacement fields $u_{above}(x)$ and $u_{below}(x)$ correspond to the displacement of the atomic rows situated at x in the planes contiguous to the glide plane above and below, respectively. The continuous variation of such fields is obtained through the spline of the discrete atomic row positions. In Fig. 2, the disregistry function has been plotted for the edge and the screw dislocations. The PN model, accounting for the formation of partial dislocations reads as follow:

$$D(x) = \frac{b}{2\pi}\left[\arctan(\frac{x-d/2}{\zeta}) + \arctan(\frac{x+d/2}{\zeta})\right] + \frac{b}{2}, \qquad (1)$$

where b is the Burgers vector of the whole dislocation, ζ the half of the width over which the partial dislocation core spreads and d is the dissociation distance between partials. While b is fixed, ζ and d have been adjusted such that the model agrees satisfactorily with the AS results. In the following, the subscripts e and s indicate the parameter values associated with edge and screw dislocation, respectively. We found for the separation distance between partials $d_e = 5.57$ b, $d_s = 2.76$ b, and for the dislocation core widths $\zeta_e = 1.2$ b and $\zeta_s = 0.69$ b. Note that although the potential used in the present work is known to provide a reasonable stacking-fault energy for Aluminium, it has been shown recently by density-functional theory calculations [39] that it overestimates the dissociation distance between the two Shockley partial dislocations. In order to minimize the finite size effects of simulations, L_x and L_z were chosen large enough to obtain a steady dislocation core geometry, i.e., with negligible variations on d and ζ when L_x or L_z vary.
According to elastic theory of dislocations [24], the dissociation distance d should be 11.5 Å for the edge dislocation and 5 Å for the screw one. Though such predictions underestimates stringently the AS results, the ratio between d_e and d_s is

qualitatively good. The PN model also predicts a ratio $\zeta_e/\zeta_s = 1/(1-\nu) = 1.47$ where ν is the Poisson's ratio [1] and in AS, it is found that $\zeta_e/\zeta_s = 1.8$. The extensions of the PN model [36, 40] could certainly allow to improve the theoretical predictions for d and ζ and to get them closer from AS data.
The adjustment of the disregistry function $D(x)$ allows us to compute the position of the partial dislocations. To such a purpose a standard manner in AS consists in analyzing the first neighbour shell [13, 18, 31, 32] of each atoms and to retain only the ensemble of atoms which the first neighbours arrangement differs from the perfect crystal. With the disregistry function, the location of the leading and trailing partials are recognized as the maximum of the first derivative of the $D(x)$ function. This method will also be applied to bowing dislocations after slicing the crystal perpendicularly to Y-axis and repeating the disregistry function adjustment in each slice. The advantage of such a method is to provide directly a smooth continuous profile for the partial dislocations.
Within AS, the straight dislocation starts to move when the applied stress τ_{app} reaches the Peierls stress $\tau_{\rm p}$ which for the edge dislocation is found $\tau_{{\rm p}e} = 1.98$ MPa while for the screw $\tau_{{\rm p}s} = 18.43$ MPa.

2.3. *Line tension of the model dislocations*

The line tension is an important property of dislocations which characterizes their stiffness along the dislocation line. It enters amongst the input parameters in the SSH analytical models. Through AS, it is not possible to compute directly the line tension. Instead the AS can be used to analyze the dislocation shape when it is anchored on some obstacles. Under a certain applied stress, the dislocation bows out indicating how stiff is the dislocation. To quantify the line tension, we shall analyze the dislocation shape given by AS within a harmonic elastic string model, also dubbed *line tension model* [41]. The simplest configuration is to consider a dislocation pinned by a regular array of obstacles, i.e., where the distance between nearest obstacles is constant. In the AS, because of PBC along Y, the introduction of a single isolated obstacle allows us to construct such a regular array with a distance between nearest obstacles fixed by L_y [32].
The anchored configurations of the different dislocations are computed for different applied stresses. In order to cover a broad range of dislocation configuration, i.e., from small to large values of L_y and τ_{app}, we introduce in AS some unshearable obstacles by freezing the position of two first neighbour atoms that cross the glide plane. Thence, the dislocation can form large bows (see Fig. 4) when L_y and τ_{app} are both large or it can be nearly straight when L_y or τ_{app} are small. We assume that the partial dislocations are tightly bounded and we analyze the mean dislocation shape by averaging the position of partial segments. This allows us to consider a single isolated dislocation anchored as represented schematically in Fig. 3 (a). In the dislocation glide plane, the point O refers to the abscissa of the dislocation apex and the bowing-out amplitude is h. The applied stress σ yields a Peach-Koehler force, $(\sigma.\vec{b}) \times \vec{\xi}$ giving the force per unit length exerted on the dislocation segment which the direction is fixed by the unitary vector $\vec{\xi}$. The Peach-Koehler force exerted in the glide direction X can be reduced to τb where τ corresponds to the resolved shear stress parallel to the Burgers vector. A segment of length L reaches equilibrium when the stress field σ is balanced by a tension $\Gamma\vec{\xi}$ at some point

[1] The shear modulus is the one for $(1\bar{1}1)$ planes $\mu = (C_{11} - C_{12} + C_{44})/3$ while Poisson's ratio is computed from the Voigt average $\nu = (C_{11} + 4C_{12} - 2C_{44})/(2(2C_{11} + 3C_{12} + C_{44}))$. Within EAM model for Al, $\mu = 30.8$ GPa and $\nu = 0.32$.

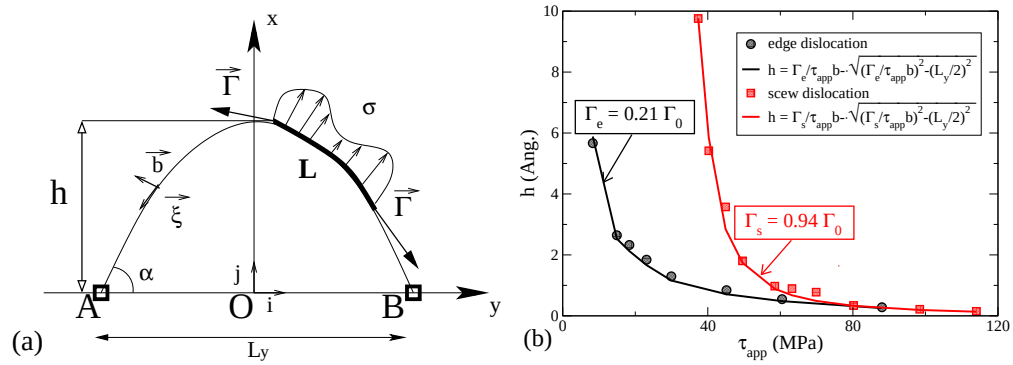

Figure 3. (a) Schematic view of the forces acting on a bowed-out dislocation between pinning centers. (b) Amplitude of bowing-out h for the pinned dislocation against the external applied stress τ_{app}, for different dislocation lengths, Ly. The circle (square) symbols correspond to the simulated edge (screw) dislocation while the lines are the adjustments of the line tension relation given in equation 3.

along the dislocation line. In order to determine the dislocation equilibrium shape in the form $x = f(y)$, we assume that the shear stress is constant discarding the self-stress field of the dislocation and those of periodic images. The Peierls stress is also assumed to be negligible. Therefore, we can use the classical result that a pinned dislocation with a constant line tension subjected to a constant stress takes a circular shape [4, 42, 43]. With the geometry shown in Fig. 3 and the boundary conditions $x(-L_y/2) = x(L_y/2) = 0$, the dislocation shape is then given by:

$$x(y) = \sqrt{R^2 - y^2} - \sqrt{R^2 - (L_y/2)^2}, \tag{2}$$

where $R = \Gamma/\tau_{app}b$ is the radius of the arc. The maximum amplitude of the dislocation bow is $h = x(0)$ which reads:

$$h(\tau_{app}, L_y) = R - \sqrt{R^2 - (L_y/2)^2}. \tag{3}$$

The effective line tension of the dislocation is determined by adjusting Γ in Eq. 3 to find the same amplitude h of the dislocation bending than in AS. The adjustment of Γ has been carried out for several dislocation configurations, i.e., for different applied stresses τ_{app} and lengths L_y. It proves to match for all configurations tested, provided that τ_p remains small with respect to τ_{app}. For different applied stress and for different types of dislocation, the dislocation bow amplitudes were reported in Fig. 3 (b) as symbols for the AS computations and as continuous lines for the analytical estimate of Eq. 3 computed from the fit of Γ.We point that the variation of h with τ_{app} is better reproduced if instead of L_y in Eq. 3 we substitute $(L_y - b\sqrt{3})$ for the edge and $(L_y - b)$ for the screw dislocation. This substitution accounts for the obstacle width in the distance between the dislocation pinning centers. In what follows the line tension will be normalized by its classical estimate given by Nabarro $\Gamma_0 = 0.5\mu b^2$ [44]. After adjusting Γ as proposed previously, the line tension predictions for the mean dislocation profile derived from Eq. 3 agree satisfactorily with AS as shown in Figs. 4 (a) and (b) for the two dislocation characters. Some small discrepancies can be noticed for the screw dislocation in Fig. 4 (b) arising from the non-negligible screw Peierls stress. The periodic potential landscape either pushes or retains locally the screw segments along the dislocation line according to their positions. The line tension estimated here has therefore to be considered as an average value over the explored configurations. As expected from dislocation theory [24], the screw dislocation is found stiffer than the edge

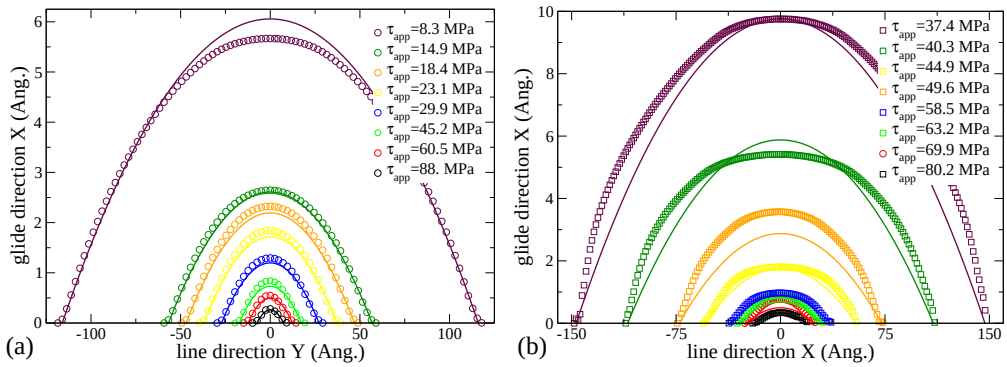

Figure 4. Comparison of the bow-out obtained by atomic-scale calculation (symbols) and line tension approximation (lines) given by Eq. 3 for edge (a) and screw (b) dislocations. Note that the scales are not the same in abscissa and in ordinate so that the dislocation position deviates from a circular shape.

one. Numerically, we obtained $\Gamma_e = 0.21\Gamma_0$ and $\Gamma_s = 0.94\Gamma_0$. One should also note that for large amplitude of dislocation bows, the effective line tension must diverge from the current estimates since the interactions between periodic images have been discarded in the present model.

Vijay et al. in [45] computed the screw dislocation line tension in Al and they account theoretically for fixed boundary condition in a cylindrical cell which radius is comparable to the height, L_z, of our simulation cell. They found $\Gamma_s = 0.84\Gamma_0$ which despite very different boundary conditions is close from our one.

The standard analytical expression for the dislocation line tension is also derived from the elasticity theory [4, 24, 42]. It reads as a function of the angle β between the Burgers vector and the tangent to the dislocation line:

$$\Gamma_{el} = \frac{\mu_{SB} b^2}{4\pi(1-\nu_{SB})} \left[(1+\nu_{SB})cos^2\beta + (1-2\nu_{SB})\sin^2\beta\right] \ln(\frac{R}{r_0}), \qquad (4)$$

where μ_{SB} and ν_{SB} are the elastic modulus following the Scattergood and Bacon definition [46] that takes into account the crystal anisotropy [1]. In the AS, the upper cut-off length, denoted by R, corresponds to the distance to the free surfaces, i.e., the half-height of the simulation box $L_z/2$. In order to obtain a line tension approximation as accurate as possible, we calculate Eq. 4 with a core radius estimated from the dislocation core half-width ζ, as computed previously. Following Hirth and Lothe in [24], for the edge character $r_{oe} = 2\zeta_e/\exp(1+\gamma)$ and for the screw one $r_{os} = 2\zeta_s/e$ where $\gamma = (1-2\nu)/(4(1-\nu))$. We obtain from Eq. 4: $\Gamma_e = 0.17\Gamma_0$ and $\Gamma_s = 0.84\Gamma_0$ which is found to be in fair agreement with the results yielded through our previous adjustment procedure.

3. Dislocation obstacle interaction

According to the SSH theory [2–4, 6–8], an obstacle can be characterized by a maximum pinning force and a finite interaction range, here denoted by f_m and w, respectively. Following the method developed in Ref. [32], these parameters are determined for different positions of an isolated Mg substitutional atom near the glide plane and for Mg dimers with different orientations of the Mg-Mg bond. Atoms of Mg are substituted to atoms of the pure Al crystal in the obstacle geometry that

[1] Using the sextic theory presented in [24], we found $\mu_{SB} = 31.9$ GPa and $\nu_{SB} = 0.34$ within the EAM model for Al.

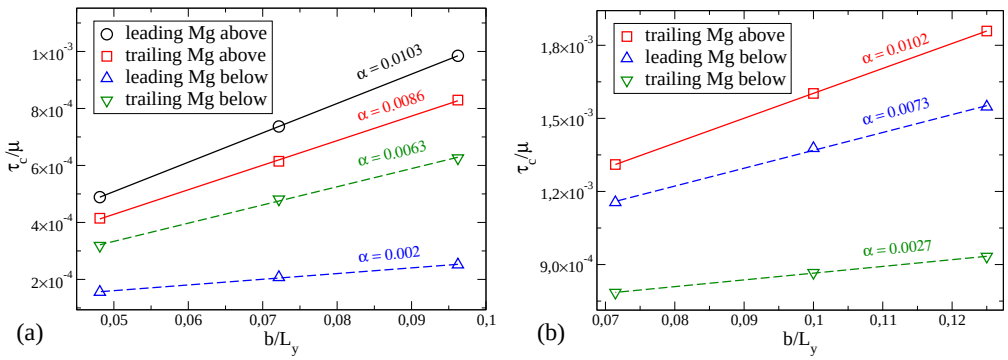

Figure 5. The normalized critical stress, τ_c/μ, versus the normalized inverse distance between pinning centers along the dislocation line, b/L_y, for Mg atom situated in the vicinity of the glide plane, and for edge (a) and screw (b) dislocations. According to Eq. 5, the linear interpolations of the critical stress associated with the leading and trailing partials are represented as continuous lines for the obstacle situated in the $(1\bar{1}1)$ plane just above the glide plane whereas dashed lines correspond to Mg in the $(1\bar{1}1)$ plane just below the glide plane.

we want study. The PBC along the dislocation line yields a chain of regularly spaced obstacles.

3.1. *Maximum pinning forces*

The Peach-Kohler force per unit length, $\tau_{app}b$ applied to the dislocation pushes it toward the Mg obstacle. The applied stress is incremented by 0.002 MPa and for each increment the crystal enthalpy minimization is repeated until either it converges to a required precision or the dislocation starts to glide. The critical threshold of the applied stress, τ_c, depends on the distance between the nearest obstacles, i.e., L_y owing to the PBC along the dislocation line. Actually a mere balance sheet of forces leads to the relation $\tau_{app}bL_y = f_m$ and therefore varying L_y and computing the corresponding critical stress within AS allows us to determine the obstacle pinning strength [32].
The previous considerations discard the pure crystal strength. Since in the atomistic model used here for Al, the dislocation has a non-negligible Peierls stress we must examine how the pure crystal strength combines with the obstacles. At the critical threshold, the force total balance sheet yields:

$$\tau_c bL_y = f_m + \tau_p^{eff} bL_y \tag{5}$$

where, in the right hand side, one recognizes the pinning strength f_m and the effect of the Peierls potential which we introduce as an effective stress τ_p^{eff} which depends on the critical profile of the dislocation and the Peierls landscape. In the limit of small L_y, the dislocations are nearly straights meaning that we can consider that the Peierls potential exerts a constant stress along the dislocation line (see appendix A). To compute the dislocation-obstacle interaction, we thus used simulation cells with small L_y, ranging from $L_y = 8$ b to 16 b.

In Fig. 5, the results of the critical stress computed from AS has been reported for different L_y for both dislocation types and both partial dislocations crossing an isolated Mg solute. We note that the AS results for short L_y are correctly reproduced by choosing τ_p^{eff} as constant in Eq. 5. This allows us to determine f_m in the limit of small L_y. The pinning coefficient, $\alpha = f_m/\mu b^2$, corresponds to the slop of the linear interpolations of the stress threshold reported in Fig. 5 (a) and (b) for different types of obstacle. Our results for the pinning strength associated with each partial dislocation have been reported in Tab. 1 with same notations as

in Ref. [18]. In Tab. 1 the single obstacle denoted by (a) corresponds to an isolated Mg placed in the $(1\bar{1}1)$ plane situated just above the glide plane and (b) is for a Mg which participates to the $(1\bar{1}1)$ plane just below the glide plane.
From Tab. 1, we found that the pinning strength depends on the position above or below the glide plane and which partial is concerned as well. Such a feature is thought to stem from the nonlinearity of the atom interactions. The anharmonicity enhances the pinning strength in the compressive regions by contrast to the tensile regions where the pinning strength is smaller.
This trend has been noticed for both edge and screw dislocations. The pinning strengths of edge dislocation are found to be larger for Mg situated above the glide plane ((a) in Tab. 1), i.e., the compressive regions in our simulation cell, than those below ((b) in Tab. 1). In agreement, for the screw type, in which the compressive region alternate for each partial according to the direction of the edge component of the Shockley partial Burgers vector, the trailing (leading) partial for Mg situated above (below) is anchored more strongly than the leading (trailing) partial for which the pinning coefficient even vanishes.

So far we have studied the anchoring forces of isolated solute atoms however, in a solid solution of few atomic percent, solutes are no longer isolated and often form clusters. In their experimental work on copper alloys Wille et al. [47] deduced the density of the discrete glide barriers. They put arguments forward that mainly doublets and triplets of solutes represent the effective glide barriers in the solid solution. The existence of a distribution of barrier strengths was revealed. This seems to be reasonable because not only single solute atoms but also pairs, triplets and multiplets of solutes can behave as different obstacles. Anisotropic barriers such simple solute pairs will interact with dislocations with a strength depending on the mutual orientation of both dislocation and obstacle. The question of whether small clusters can play a role in SSH was addressed by AS in Ni(Al) [32] and Fe(Cu) [16]. It was shown that the strongest pairs which may be relevant to describe the SSH rate differ from each alloys. In order to question again these features for Al(Mg) system as well as to evolve toward a higher-scale model that will permit analysis of the SSH at high Mg concentration, a systematic study of the dislocations/dimers interaction was performed. The pinning strengths of the Mg dimers have been calculated with distances between Mg atoms that correspond to first ((n-p) in Tab.1), second ((k-m) in Tab.1) and some of the third neighbour ((i-j') in Tab.1). Either the dislocation interacts with pre-existing Mg dimers referred to as (c-h) in Tab.1 or else the dislocation passage modifies the Mg-Mg bond crossing the glide plane (i-p) in Tab.1. For the non-crossing pairs, the (c-e) and (f-h) configurations correspond to the planar dimer situated above and below the glide plane, respectively. The interaction parameters for Mg pairs reported in Tab. 1 show a wide scatter depending on the obstacle configuration and of the partial dislocation considered. We will discuss in more detailed way their scaling relations in subsection 3.3.

3.2. *Interaction range*

To compute the interaction ranges the variation of the internal energy of the nanocrystal is recorded during a simulation with a constant applied stress fixed to the critical threshold that corresponds to the type of obstacle present in the simulation cell. For both dislocation characters, such energy variation has been reported in Figs. 6 (a) and (b) for an isolated Mg situated in the nearest $(1\bar{1}1)$, either below or above the glide plane. The internal energy is computed from the sum of the atomic potential energy in the course of the enthalpy minimization procedure. During the interaction between a dislocation and a solute atom calculated via an over-damped

Table 1. Summary of different pinning obstacles for both the leading (subscript l) and the trailing partials (subscript t) of the edge and screw dislocations, the bond orientation of the pair, their pinning force α normalized by μb^2, and their interaction range w.

Nature	Text ref.	pair orientation	Edge α_l and w_l	Edge α_t and w_t	Screw α_l and w_l	Screw α_t and w_t
Single	(a)		0.0103/5.11b	0.0086/2.16b	0.0000/0.b	0.0102/1.81b
	(b)		0.0020/0.24b	0.0064/3.69b	0.0073/2.96b	0.0028/2.38b
1st neighbor	(c)	$[011]$	0.0170/4.72b	0.0159/2.65b	0.0000/0.b	0.0228/1.74b
Noncrossing	(d)	$[10\bar{1}]$	0.0177/5.29b	0.0158/1.95b	0.0000/0.b	0.0224/1.61b
pair	(e)	$[110]$	0.0128/5.31b	0.0129/2.15b	0.0000/0.b	0.0228/1.54b
	(f)	$[01\bar{1}]$	0.0000/0.b	0.0103/3.94b	0.0080/1.48b	0.0051/2.87b
	(g)	$[10\bar{1}]$	0.0000/0.b	0.0122/3.66b	0.0081/1.63b	0.0060/2.83b
	(h)	$[\bar{1}10]$	0.0000/0.b	0.0082/4.18b	0.0152/1.96b	0.0086/2.27b
3rd neighbor	(i)	$[721]$	0.0062/0.74b	0.0139/2.83b	0.0138/0.69b	0.0026/1.21b
Crossing pair	(j)	$[21\bar{1}]$			0.0038/0.95b	0.0112/0.95b
	(j')	$[27\bar{1}]$	0.0062/1.75b	0.0145/2.11b		
2nd neighbor	(k)	$[212]$	0.0100/1.06b	0.0099/2.96b	0.0045/0.68b	0.0110/0.60b
Crossing pair	(l)	$[\bar{1}2\bar{2}]$	0.0102/1.87b	0.0103/1.86b	0.0064/0.98b	0.0062/0.85b
	(m)	$[2\bar{2}\bar{1}]$			0.0064/0.98b	0.0025/1.83b
1st neighbor	(n)	$[4\bar{1}1]$	0.0067/2.18b	0.0120/2.59b	0.0043/1.06b	0.0119/0.61b
Crossing pair	(o)	$[1\bar{1}4]$	0.0061/1.06b	0.0086/2.93b	0.0054/0.68b	0.0141/1.09b
	(p)	$[\bar{1}4\bar{1}]$	0.0065/1.15b	0.0106/1.83b	0.0032/0.84b	0.0033/0.94b

noiseless Langevin dynamics, the total energy of the system can be decomposed into three parts: the elastic energy, the line energy and the energy of dislocation-solute interaction. As the applied stress is constant, the energy variation shown in Figs. 6 is due solely to the line and the interaction terms. The former is however negligible for the short dislocation segment simulated here. Figs. 6 represents the energy landscape felt by a dislocation during the crossing of an obstacle. An important point of this procedure is to choose a friction in the atomic equation of motion well above the work due to the applied stress so that it does not cause heating.

In Fig. 6 (a), for an Mg atom situated above the glide plane, the potential energy shows two peaks that correspond to the successive passage of the two partials on the obstacle. The same is also noticed for the screw dislocation and for different positions of the solute atom. By contrast, for an Mg atom situated below the glide plane, the interaction with the edge dislocation can no longer be separated in two distinct contributions but the interaction spreads over the whole sacking fault ribbon. It is worth noticing that the interaction potential is not symmetric for an obstacle ahead and behind the partials, mainly because of the stacking fault region.

Even though the shape of the interaction potential involves nonlinear atomic interactions, the interaction can be qualitatively understood in terms of the linear elastic theory of dislocations. As reported in Fig. 6 (a), an isolated solute situated above the glide plane repeals edge dislocation whereas the same Mg atom below acts as an attractive obstacle. Hence, it seems reasonable that hydrostatic stress field dominates the interaction since Mg solute behaves as a dilatation center in Al matrix. The same explanation holds for the screw dislocation in Fig. 6 (b) where tensile and compressive regions alternate following the edge part of the Shockley partial Burgers vectors. The internal energy is derived with respect to the average position of the dislocation. In Figs. 7 (a) and (b), such quantity which corresponds to the internal force of the crystal has been plotted against the mean dislocation position. A negative value means that the dislocation is pushed forward while a positive one corresponds to a force that retains the dislocation. Many different maxima appears along a same curve indicating that for a given type of obstacle different pinning configurations are possible and may contribute to anchor the dislocation in a complete solid solution. In Figs. 7 (a) and (b), our estimate of the

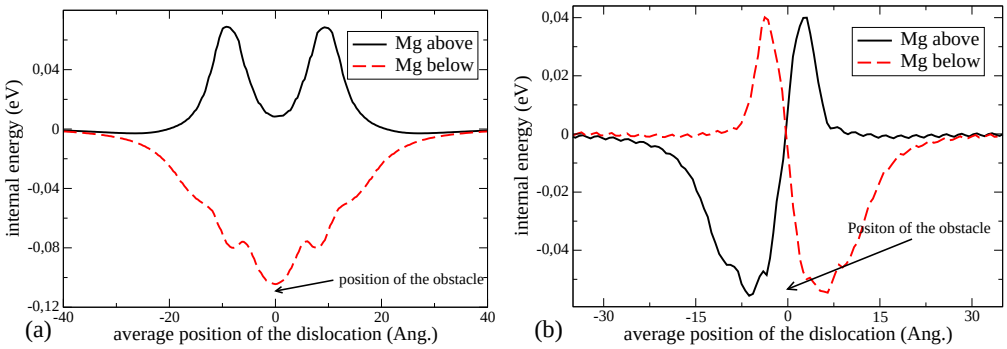

Figure 6. Internal energy of the simulation box versus the average position of the edge (a) and the screw (b) dislocation core. The simulation box contains a single obstacle formed by one isolated Mg solute atom situated either in the plane above the glide plane (full line) or the plane below the glide plane (dashed line).

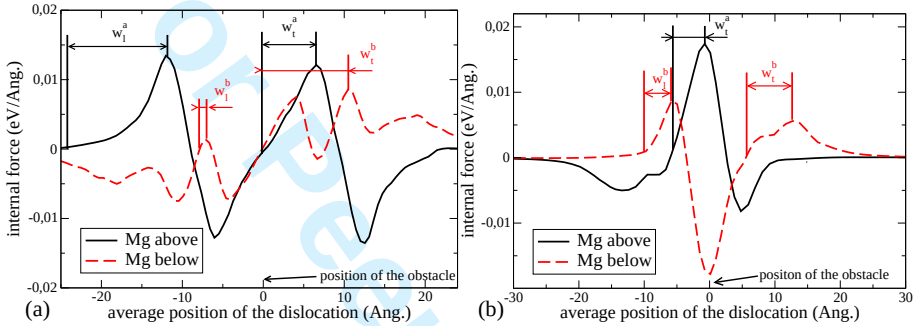

Figure 7. Internal force versus dislocation average position: the derivative of the internal energy of figure 6 for an edge (a) and a screw (b) dislocation. The full and dashed lines correspond to obstacles formed by one isolated Mg solute atom situated in the plane above (see w(a) in Tab. 1) and below (see w(b) in Tab. 1) the glide plane, respectively.

interaction extent is exemplified. The range of interaction is estimated from the distance which separates the maximum of the force and the nearest position for which the force vanishes. Our results for the interaction ranges have been reported in Tab. 1 with same notations as in Ref. [18].

We obtain some interaction ranges in average larger for the edge dislocation than for the screw one. The interaction extent, computed for the non-crossing pairs ((c-h) in Tab. 1) are roughly equal to the range of the isolated solutes while the one of crossing pairs is smaller ((i-p) in Tab. 1). We examine how connect these pair interaction ranges with some physical core features of dislocations in the next subsection.

3.3. *Scaling relations for the dimer interaction parameters*

In order to identify the origin of the differences in SSH between Al(Mg) and Ni(Al) alloys, it is of some interest to compare the dimer pinning strength in Al(Mg) with those in Ni(Al) as the ordering energy of the latter is much higher and indicates the possibility of an important chemical effect [48]. In fact, a dislocation shearing a cluster by a Burgers vector shifts the solutes on either side of the slip plane, which can lead solutes in a configuration less favourable energetically increasing their pinning strengths. This is the case of alloys with a significant short-range order. In the Ni(Al) alloy and through solute pair interactions, this effect has been invoked in [13, 32] to tentatively explain the nearly linear CRSS against the solute concentration. The comparison of the dislocation pinning strength of pairs could

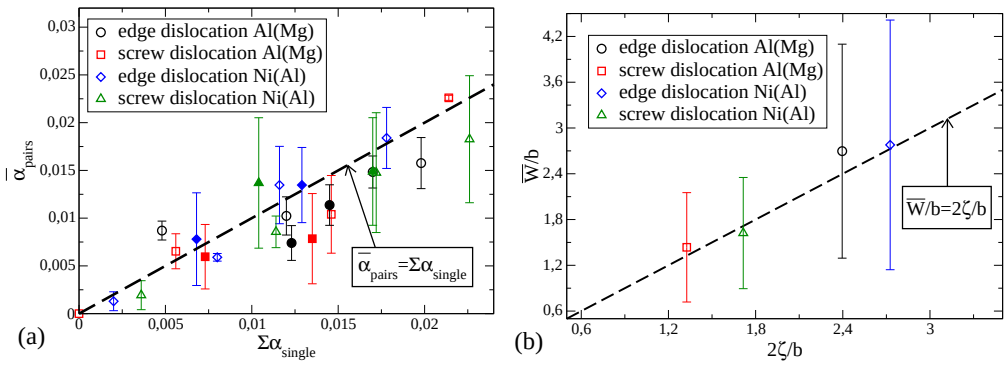

Figure 8. (a) Average pinning coefficient of solute dimers as a function of the linear combination of the pinning strength of two isolated solutes which the superimposition corresponds to the dimer. The solute dimers that cross the slip plane are represented by full symbols while open symbols are used for those that do not cross the slip plane. (b) Normalized interaction range averaged over all the obstacle geometries against the normalized dislocation core widths for both dislocation segments edge and screw. The results for two different fcc alloys are presented: Mg solutes in Al (present work) and Al solutes in Ni from Ref. [18, 32]. In each graph the straight dashed line represents equality between abscissa and ordinate.

then provide us some hint on how such chemical effect could modify the hardening mechanism in the different alloys. To perform this comparison we use the data relative to the dimer-dislocation interactions in Ni(Al) from Ref. [18, 32].

As in Ni(Al), the pinning strengths and the interaction ranges of Al(Mg) pairs reported in Tab. 1 span on a wide spectrum of values making difficult to identify clearly some trends concerning the solute pairs effect. To rationalize the behaviour of dimers, we compare their pinning strengths with the ones of isolated solute atoms. We compute the average pinning coefficient of solute pairs, $\bar{\alpha}_{pair}$, and the corresponding linear combination of the isolated solute pinning coefficients, $\sum \alpha_{single}$. For instance, the average pinning coefficient for first neighbour pairs situated above the slip plane is compared with the twice of the pinning coefficient for a single solute situated above the slip plane. For each partial dislocation in both alloys and for edge and screw dislocations we thus compare:

$$\begin{aligned} \bar{\alpha}_{\text{1st neighbour noncrossing pair above}} &\text{ with } 2\alpha_{\text{single above}}, \\ \bar{\alpha}_{\text{1st neighbour noncrossing pair below}} &\text{ with } 2\alpha_{\text{single below}}, \\ \bar{\alpha}_{\text{crossing pair}} &\text{ with } \alpha_{\text{single above}} + \alpha_{\text{single below}}. \end{aligned} \tag{6}$$

The results of this comparison are shown in Fig. 8 (a). In both model alloys and for both dislocation characters, we observe a fairly good correlation between the average pair coefficients and their description in terms of isolated solute linear combination. On average, the strongest pairs are merely formed by solutes that have the largest pinning strengths in agreement with Ref. [16]. The largest pinning strengths are found in both alloys for the noncrossing pairs located in the compressive stress fields of dislocations. This result reflects the effect previously described for isolated solute atoms for which the pinning strength magnitude differences can be mainly attributed to the anharmonic effect.

On Fig. 8 (a), it is worthy to note that there is no apparent difference between noncrossing (open symbols) and crossing pairs (full symbols) even for the Ni(Al) alloy where the chemical effect is expected to have some influence. Such a result points the lack of clear chemical strengthening effect at least if we reason in terms of maximum pinning strength of obstacle, following the analytical models.

A second essential parameter used in the formulation of SSH analytical models is the interaction range of obstacles. For obstacles formed by dimers of solute

atoms, these ranges show a deviation from the classical estimate equal to b as reported in Tab. 1. As for the pinning coefficients, we observe a broad range of w, distributed around a typical value of $2b$. We note that the interaction ranges associated with the edge dislocations is on average greater than that for screw dislocations. Similarly, for the same character of dislocation, they are larger in Ni(Al) than in Al(Mg). To understand these trends, we choose to think in terms of average ranges, $\overline{W}$. For each dislocation type in both alloys, we define the average range as $\overline{W} = \sum_{i=1}^{n} w_i/n$ where the sum is performed on all the n obstacle configurations. As we study the interaction between dislocations and obstacles located in the vicinity of the slip plane, we choose to compare $\overline{W}$ with the dislocation core widths 2ζ computed in Sec. 2 since the variation of the internal energy is expected to arise mainly from the dislocation core-solute interactions. The comparison between these two quantities is plotted on Fig. 8 and shows a satisfactory correlation. The fact that this correlation is observed for the edge and screw dislocations in both alloys seems to indicate that the dislocation core width is a relevant physical parameter to describe a typical length scale for the dislocation-solute interactions in the dislocation glide plane.

Despite some scatters, the present work shows that there is no significant difference between the solute pair interaction parameters in Ni(Al) and Al(Mg). In both model solid solutions, the pinning forces and the interaction ranges of dimers follow in average the same scaling relations. The dimer pinning forces are found to derive on average from the linear superposition of the isolated solute force and the dislocation pinning is found to have a short range contribution related to the extent of Shockley partials. Such a result emphasizes that the mere consideration of the input parameters of SSH analytical models, even extended for the dimers, is not sufficient to distinguish a priori the SSH rates in Ni(Al) and Al(Mg). We thus expect that the CRSS of both alloys increases similarly with the solute concentration.

4. Solid solution hardening statistics

We now address directly the SSH by computing the CRSS of a dislocation in the solid solutions with different concentrations. We perform some static AS for the edge and the screw dislocation gliding in a Al(Mg) random solid solution and we derive from the statistical study of such AS the CRSS as a function of Mg contents. The AS allow us to test the predictions from the analytical SSH theories in which the impurities are assumed to be randomly distributed in the glide plane. For the two dislocation characters, we compare our results with those obtained in Ni(Al) [18, 32].

4.1. *Molecular static computation of the solid solution pinning strength*

In order to calculate the CRSS of a solid solution, we replicate the methodology developed in [32] for the edge dislocation gliding in some random Ni(Al) solid solutions. These static simulations are similar to those implemented for determining the pinning force of a single obstacle. Once the dislocation is introduced into the crystal, we substitute randomly the Al atoms of the matrix by Mg solute atoms to achieve the desired concentration. The distribution of solute atoms is completely random and, at the end of the substitution process, the probability of finding a solute atom on an atomic site is equal to the Mg concentration, c_{Mg}. The lattice

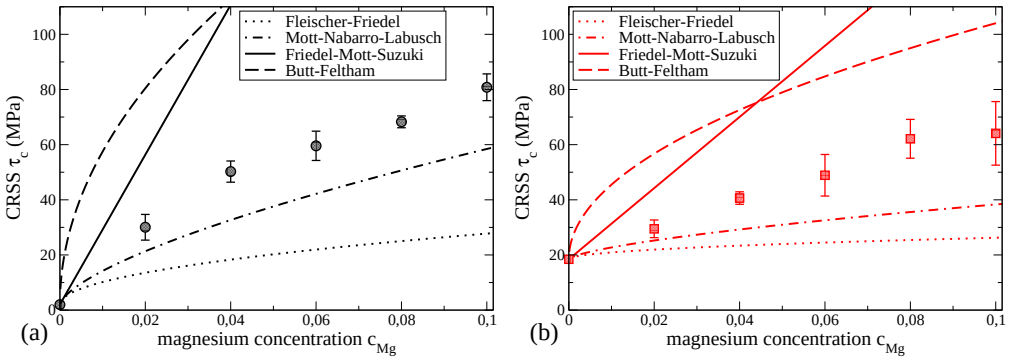

Figure 9. Variation of the critical resolved shear stress (CRSS), τ_c, for an edge dislocation (a) and for a screw dislocation (b) against the Mg concentration, c_{Mg}, computed from the atomic-scale simulations (AS) with different Mg random distributions (symbols). The error bars correspond to the standard deviation. The estimations made from the analytical models (see Tab. 2) have also been reported: Fleischer-Friedel [3] (dotted line), Mott-Nabarro-Labusch [51] (dot-dashed line), Friedel-Mott-Suzuki [4] (full line) and Butt-Feltham [6] (dashed line).

parameter varies with the solute concentration following Vegard's law. After an initial relaxation of the potential energy of the system, we apply a stress on the crystal surfaces by increments of 4 MPa. After each stress increment, the enthalpy of the system is relaxed until the dislocation encounters a stable position or glides in the solid solution. The flow stress decreases with the length of the dislocation line. It converges toward an asymptotic flow stress of which dispersion is much larger than its variation with L_y. To reach this asymptotic behaviour we simulate extended dislocation segments up to $L_y = 520b$ for the edge and $L_y = 300b$ for the screw dislocations. The dislocation crosses several times the simulation box owing to the PBC in the glide direction. At each passage, the dislocation shears the crystal by one Burgers vector creating a new configuration of solute atoms. We therefore simulate the equivalent of a dislocation gliding in an extended solid solution with random solute distribution.

For a certain stress level, the dislocation no longer encounters stable configurations during its pseudo-dynamic and moves freely in the alloy. This stress corresponds to the calculation of the critical flow stress, τ_c. However its level depends on the distance travelled by the dislocation. Indeed, the longer is the dislocation travel the higher is the probability to encounter a pinning configuration.[49, 50] We choose a glide distance at least equal to 1000 Å. The CRSS is then considered as the stress required for the dislocation to glide over this distance, corresponding to the order of magnitude of one tenth of the average distance between dislocations in an annealed polycristal. The applied stress increases sharply at the beginning of the glide and quickly reaches a plateau near the CRSS. In practice, the stress does not increase for a glide distance larger than 500 Å, equivalent to about 5 simulation box lengths.

We study the variation of τ_c for the two types of dislocation as a function of the solute concentration for an atomic concentration ranging from $c_{Mg} = 2$ at.% to 10 at. %. The CRSS increases with c_{Mg} because of the increased density of obstacles. Unlike the calculations for the interaction between a dislocation and an isolated obstacle giving us τ_c deterministically, the SSH simulations require several realizations. For each concentration τ_c is calculated from an average over a sampling of five simulations. The CRSS of the Al(Mg) solid solution are reported for the edge and screw dislocations in Fig. 9 (a) and (b), respectively. The average flow stress as a function of concentration is monotonic and smooth. This variation is greater than the standard deviation of the flow stress (see error bars on Fig. 9) except for the screw dislocation at the highest concentration. Using the Peierls stress τ_p calculated

Table 2. Summary of solid solution hardening (SSH) analytical models reviewed in [18]. The critical resolved shear stress (CRSS), τ_c, is expressed as a function of the line tension, Γ, the pinning strength, f_m, the interaction range, w, the solute concentration, c, the Burgers vector, b, and the atomic surface in the $(1\bar{1}1)$ dislocation slip planes, s.

Model:	Fleischer-Friedel [3]	Mott-Nabarro-Labusch [51]	Friedel-Mott-Suzuki [4]	Butt-Feltham [6]
τ_c :	$\frac{f_m^{3/2}\sqrt{c}}{b\sqrt{2s\Gamma}}$	$\left(\frac{c^2 2w f_m^4}{b^3 s^2 \Gamma}\right)^{1/3}$	$\frac{f_m w c}{sb}$	$\frac{4 f_m w \sqrt{c}}{3b^3}$

in Sec. 2, the phenomenological equation $\tau_c = \tau_p + Ac_{Mg}^r$ has been used to fit the CRSS computed from AS. The exponent that provides the best fit is $r \simeq 2/3$ for the edge dislocation and $r \simeq 4/5$ for the screw dislocation. This result contrasts with the one obtained in [18, 32] for Ni(Al) alloy which showed an almost linear dependence on concentration with r close from unity for both dislocation types. However, as in Ni(Al), the AS show that the pinning strength is of same order for the screw dislocations and for the edge ones, in agreement with the pinning strengths of isolated obstacles computed in Sec. 3. Even though we subtract the Peierls stress to keep only the hardening effect of solutes, the screw dislocation CRSS is at least twice smaller than τ_c of the edge dislocation. It is a remarkable result because it confirms that the screw dislocations undergo a significant pinning in the solid solution as already found in Ni(Al)[18].

4.2. *Comparison between analytical models and atomic-scale simulations*

The previous AS for the random solid solution correspond to the theoretical framework of the SSH analytical models (see Tab. 2). The latter assume actually a perfectly random distribution of impurities at zero temperature which is also the case in our simulations. The parameters of the different models, i.e., Γ, f_m and w have been determined through AS in Sec. 2 and 3.

Following our previous work [18], we adapt the analytical models to the fcc solid solution where the dislocations are dissociated into 2 partial dislocations. As the models apply to an undissociated dislocation, we assume that the partial dislocations are tightly bounded. Moreover, the different models usually derived for a square lattice assumes an atomic area in the slip plane equal to b^2. In our system, this quantity is changed to $s = b^2\sqrt{3}/2$, i.e., the atomic surface in the $(1\bar{1}1)$ dislocation slip planes. The effective obstacle concentration corresponds to $4c_{Mg}$ in order to take into account all the interactions of both partial dislocations with the single solutes above and below the slip plane. In the derivation of the Mott-Nabarro-Labusch model, the solutes above and below the slip plane are already taken into account. In this particular case we must replace c_{Mg} by $2c_{Mg}$.

The analytical models consider a single type of obstacle, thought of as an average obstacle which would lie in the glide plane, disregarding the long range interactions between the dislocation and the solute atoms. The manner how the average obstacle is computed from the different atomic configurations is not stipulated in the SSH theories. We saw in Sec. 2 and Sec. 3 that an important contribution to the pinning strength stems from the obstacles situated in the $(1\bar{1}1)$ planes that bound the glide plane. Only the latter are considered in our estimation for the strength and the interaction range that characterize the average obstacle. As previously mentioned, there are four possible interactions between a dislocation and an isolated solute atom in accordance with its position and the partial dislocation with which it interacts. To consistently compare the predictions of our AS with the SSH models, the input parameters are determined from the average of the isolated atoms interaction parameters (see obstacles (a) and (b) in Tab. 1). We get an average pinning coefficient $\bar{\alpha}_e = 0.0068$, $\bar{\alpha}_s = 0.005$ and an average interaction

range $\bar{w}_e = 2.8b$, $\bar{w}_s = 1.8b$ for a single Mg solute atom situated in one $(1\bar{1}1)$ plane adjacent to the slip plane.

From the equations reported in Tab. 2, we plot in Fig. 9 the CRSS as a function of the Mg concentration for the four SSH models. For both dislocation types the Fleischer-Friedel (FF) model predicts the smallest flow stress. The predictions from the Mott-Nabarro-Labusch (MNL) model are larger and those from the Mott-Friedel-Suzuki (FMS) model and the Butt-Feltham (BF) model still larger. Figure 9 shows that the BF and the FMS theories overestimate the CRSS whereas MNL and FF theories underestimate it. In the Al(Mg) model solid solution studied here, it seems that the MNL theory gives the best agreement with respect to our AS for both dislocation types. However we observe that the agreement between the MNL theory and the AS simulations is only qualitative. At high concentration, the CRSS of the screw dislocation is particularly underestimated due to a concentration exponent, r, larger than the one predicted in the MNL theory equal to 2/3. Note that the dispersion of flow stress is well below the differences between the predictions given by the different models. This justifies our method to compare the evolution of flow stress calculated from simulations and analytical theories.

The purpose of this study is not to predict what would be the solution hardening of the real Al(Mg) alloy, though we can expect it to be close to our atomistic results, but rather to test the analytical models available. The atomistic simulations are considered as a reference which the analytical model should reproduce to be relevant for our typical system. If the MNL theory provides a fairly good description of SSH in Al(Mg) it is not the case for Ni(Al) where the best theoretical description is given by the FMS theory [18]. The comparison between the calculated CRSS in AS and the one computed from the analytical models with no adjustable parameters shows that it is necessary to change the model as a function of the fcc alloy which is concerned. As a consequence, we are in an unsatisfactory situation where we choose a posteriori the appropriate model to describe the SSH, being unable to justify this choice. Such a result points the absence of a robust model able to quantitatively describe the SSH in fcc metals with different physical properties. Furthermore, as previously shown in the study bearing on dislocation-dimer interactions, the chemical order effect can hardly be invoked to explain alone the different SSH rates observed in Ni(Al) and Al(Mg). It therefore seems necessary to enrich the analytical models and their input parameters in order to achieve a quantitative description of SSH.

5. Summary and conclusions

The AS presented here show that in the Al(Mg) solid solutions the edge and the screw dislocations experiment similar pinning strengths. This agrees with an earlier work about the Ni(Al) solid solutions.[18] According to our informal discussions with G. Saada and D. Rodney, this result would explain why the microstructures in fcc solid solutions are isotropic, i.e., with an equivalent proportion of edge and screw dislocations [52].

From the elementary interactions computed at the atomic-scale, we have determined the input parameters required in the analytical theories for SSH. We have then compared the CRSS predictions from the different theories with the atomic-scale simulations where a nano-crystal of random solid solution with different concentrations is crossed by a single dislocation. In the Al(Mg) solid solutions studied here, the MNL theory describes qualitatively the variation of the CRSS with the Mg solute concentration. This result contrasts with our previous work about Ni(Al)

solid solutions for which the FMS model reproduced satisfactorily the AS. The two models differ stringently on the CRSS rate against the solute concentration with an effective CRSS concentration exponent $r \simeq 2/3$ in the former while $r \simeq 1$ in the latter. A comprehensive study of the pinning strength and of the interaction range associated with the different types of obstacle shows that this difference between the two systems is certainly not associated with the solute dimers alone, as it was proposed by one of us (LP) in [32]. Indeed, in the two systems, the pinning forces behave roughly as a linear combination of the strengths of individual solutes. The present study allows us to emphasize the absence of a robust analytical model, able to predict quantitatively the SSH in fcc alloys. Alongside this analytical work, an extended version of the line tension model has been proposed in order to account for the dissociation of the dislocations and for the different types of obstacle [53]. The principle of such a model have already been applied successfully to different problems [41, 54] in dislocation physics.

Acknowledgements

Dr. David Rodney is gratefully acknowledged for his fruitful remarks.

References

[1] P. Haasen *Dislocations in Solids*, Vol. 4, North-Holland, Amsterdam, 1979.
[2] N.F. Mott and F.R.N. Nabarro *Report on the Strength of Solids*, Physical Society, London, 1948.
[3] R.L. Fleischer and W.R. Hibbard, Proc. Conf. at N.P.L. 1 (1963) p.262.
[4] J. Friedel *Dislocations*, Addison-Wesley, New York, 1964.
[5] R. Labusch, Phys. Stat. Sol. 41 (1970) p.659.
[6] M.Z. Butt and P. Feltham, Phys. Stat. Sol. A 60 (1980) p.167.
[7] F.R.N. Nabarro *Dislocations and Properties of Real Materials*, The Institute of Metals, London, 1985.
[8] T. Suzuki, S. Takeuchi and H. Yoshinaga *Dislocation Dynamics and Plasticity*, Springer-Verlag, Berlin Heidelberg, 1991 32.
[9] Y.M. Blanter and V.M. Vinokur, Phys. Rev. B 66 (2002) p.132101.
[10] E. Clouet, S. Garruchet, H. Nguyen, M. Perez and C.S. Becquar, Acta Mater. 56 (2008) p.3450.
[11] X.Y. Liu, J. Wang and S.B. Biner, Modelling Simul. Mater. Sci. Eng. 16 (2008) p.045002.
[12] R.C. Picu and D. Zhang, Acta Mater. 52 (2004) p.161.
[13] E. Rodary, D. Rodney, L. Proville, Y. Bréchet and G. Martin, Phys. Rev. B 70 (2004) p.054111.
[14] K. Tapasa, D.J. Bacon and Y.N. Osetsky, Mater. Sci. and Eng. A 400 (2005) p.109.
[15] J. Marian and A. Caro, Phys. Rev. B 74 (2006) p.24113.
[16] K. Tapasa, D.J. Bacon and Y.N. Osetsky, Modelling Simul. Mater. Sci. Eng. 14 (2006) p.1153.
[17] K. Tapasa, Y.N. Osetsky and D.J. Bacon, Acta Mater. 55 (2007) p.93.
[18] S. Patinet and L. Proville, Phys. Rev. B 78 (2008) p.104109.
[19] L. X.-Y., O.P. P., J.B. Adams, C.L. Rohrer and R.W. Hyland, Surf. Sci. 373 (1997) p.357.
[20] D.L. Olmsted, L.G. Hector, W.A. Curtin and R.J. Clifton, Model. Simul. Mater. Sci. Eng. 13 (2005) p.371.
[21] D.L. Olmsted, L.G. Hector and W.A. Curtin, Jour. of Mech. Phys. Sol. 54 (2006) p.1763.
[22] W.A. Curtin, D.L. Olmsted and L.G. Hector, Nature Mater. 5 (2006) p.875.
[23] M.A. Soare and W.A. Curtin, Acta Mater. 56 (2008) p.4046.
[24] J.P. Hirth and J. Lothe *Theory of dislocations*, Wiley Interscience, New York, 1982.
[25] F. Ercolessi and J.B. Adams, Europhys. Lett. 26 (1994) p.583.
[26] X.Y. Liu, J.B. Adams, F. Ercolessi and J.A. Moriarty, Modelling Simul. Mater. Sci. Eng. 4 (1996) p.293.
[27] B.W. Person *A Handbook Lattice Spacing and Structures of Metals and Alloys*, Pergamon, New York, 1958.
[28] C. Gault, A. Dauger and P. Boch, phys. stat. sol. (a) 43 (1977) p.625.
[29] J. Zander, R. Sandström and L. Vitos, Comp. Mater. Sci. 41 (2007) p.86.
[30] N.V. Doan and R. Vascon, Nucl. Instr. and Meth. in Phys. Res. B 135 (1998) p.207.
[31] D. Rodney and G. Martin, Phys. Rev. B 61 (2000) p.8714.
[32] L. Proville, D. Rodney, Y. Bréchet and G. Martin, Phil. Mag. 86 (2006) p.3893.
[33] Y.N. Osetsky and D.J. Bacon, Modelling Simul. Mater. Sci. Eng. 11 (2003) p.427.
[34] P. Chauve, T. Giamarchi and P. Le Doussal, Phys. Rev. B 62 (2000) p.6241.
[35] H. Hakkinen, S. Makinen and M. Manninen, Phys. Rev. B 41 (1990) p.12441.
[36] G. Schoeck, Acta Mater. 54 (2006) p.4865.
[37] R.E. Peierls, Proc. Phys. Soc. 52 (1940) p.34.
[38] F.R.N. Nabarro, Proc. Phys. Soc. 59 (1947) p.256.
[39] C. Woodward, D.R. Trinkle, L.G. Hector and D.L. Olmsted, Phys. Rev. Lett. 100 (2008) p.045507.

[40] V. Bulatov and W. Cai *Computeur simulations of dislocations*, Oxford university press, Oxford, 2006.
[41] D. Rodney and L. Proville, Phys. Rev. B 79 (2009) p.094108.
[42] G. Witde and J.S. Koelher, Phys. Rev. 116 (1959) p.1113.
[43] L. Dupuy and M.C. Fivel, Acta Mater. 50 (2002) p.4873.
[44] F.R.N. Nabarro *Theory of Crystal Dislocations*, Oxford University Press, Oxford, UK, 1967.
[45] B. Vijay, B. Shenoy and R. Phillips, Phil. Mag. A 76 (1997) p.367.
[46] R.O. Scattergood and D.J. Bacon, Phil. Mag. 31 (1975) p.179.
[47] T. Wille, G. Gieseke and C. Schwink, Acta Metall. 35 (1987) p.2679.
[48] J.C. Fisher, Acta Metall. 2 (1954) p.9.
[49] L. Proville, J. Stat. Phys. 137 (2009) p.717.
[50] L. Proville, Ann. of Phys. 325 (2010) p.748.
[51] F.R.N. Nabarro, Phil. Mag. 35 (1977) p.613.
[52] A.S. Argon *Strengthening mechanisms in crystal plasticity*, Oxford University Press, Oxford, New York, 2007.
[53] L. Proville and S. Patinet, Phy. Rev. B 82 (2010) p.054115.
[54] D. Rodney and L. Proville, Phys. Rev. B 78 (2008) p.104115.

Appendix A. Association of Peierls stress and obstacle forces for large L_y

In Fig. A1 we consider the case of an Mg atom situated in the plane just above the glide plane in interaction with a screw dislocation for large L_y. For a metal with negligible τ_p, a linear relationship between $\frac{\tau_c}{\mu}$ and $\frac{b}{L_y}$ would have been obtained. Here for the screw dislocation in Al it is clearly not the case and, in the region of very large inter-obstacle distance, the results of simulations deviate from the linear Eq. 5. Note however that the AS results for short L_y are correctly reproduced by choosing a constant τ_p^{eff} close to the lattice resistance τ_p. This allows us to determine f_m in the limit of small L_y via Eq. 5 as we did in section 3.1. In this appendix, we propose to take into account the dislocation shape and the Peierls stress in Eq. 5 in order to render more accurate the model in the range of large L_y.

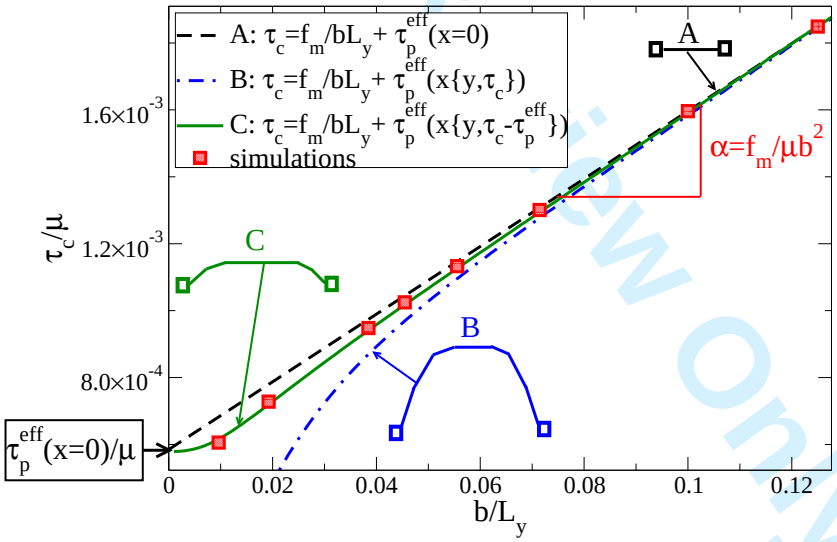

Figure A1. Normalized critical stress (square), τ_c/μ, that needs a screw dislocation to overcome an isolated Mg solute atom situated in the $(1\bar{1}1)$ plane just above the glide plane (see α(a) in Tab.1) versus the normalized inverse distance between pinning centers along the dislocation line, b/L_y. The critical stresses are computed under various assumptions regarding dislocation pinned shapes given by Eq. 2. A: flat dislocation (dashed line), B: large bending (dot-dashed line) and C: small bending (continuous line) accounting for the effective Peierls stress.

For large L_y, τ_p^{eff} depends on the critical profile of the dislocation and on the Peierls stress. For a dislocation which crosses few Peierls valleys, the critical configuration may have a larger segment on the ascent (descent) of the Peierls hills,

thereby increasing (decreasing) τ_c in Eq. 5. One can expect $0 < \tau_p^{eff} < \tau_p$ where the two bounds correspond to the two limiting cases, i.e., the depinning of a dislocation crossing several Peierls valleys or a straight dislocation retained by the maximum Peierls stress. We assume that the Peierls barrier can be roughly approximated by a mere cosine function as $V(x) = -\tau_p b a' \cos\left(\frac{2\pi}{a'}[x+\phi]\right)/2\pi$ where ϕ is a phase shift and a' is the repeat distance in the slip plane in the direction normal to the dislocation. In the present case, $a'_e = b/2$ for the edge dislocation and $a'_s = \sqrt{3}b/2$ for the screw one. The physical reason for introducing a phase shift is that the minimum of the interaction potential between the dislocation and the solute atom does not necessary corresponds to a Peierls trough. In Eq. 5, τ_p^{eff} results from the sum of crystal resistance along the curved dislocation:

$$\tau_p^{eff} = \int_{-L_y/2}^{L_y/2} \tau_p b \sin\left(\frac{2\pi}{a'}[x(y,\tau)+\phi]dy, \right. \tag{A1}$$

where the dislocation mean profile $x(y,\tau)$ is determined by Eq. 2. The computation of the integral A1 is realized numerically. ϕ is adjusted so that Eq. 5 reproduces τ_c for the shortest L_y in the case of a straight dislocation, i.e., with $x(y) = 0$. The phase shift is then kept constant to calculate τ_c for other L_y. The critical threshold is determined as a function of L_y by finding the maximum τ_c that balances the equilibrium Eq. 5. In Fig. A1, the computation of τ_c has been reported following three different approximations depending on the dislocation critical shape: a straight line with $x(y) = 0$ (model A), a large bending given by $x(y,\tau_c)$ (model B) and a small bending given by $x(y, \tau_c - \tau_p^{eff})$ (model C).

Model A: As discussed above, for large L_y, the AS results deviate from a linear relationship. The assumption of a straight dislocation leading to a linear relationship and to a constant τ_p^{eff} slightly overestimates τ_c calculated from AS.
Model B: For large L_y and for τ_c comparable with τ_p, the solution $x(y,\tau_c)$ overestimates the dislocation bending since the effect of τ_p on the dislocation shape have been disregarded in Eq. 2. Notably, this function gives dislocation shapes which fully go into the next Peierls valleys. According to the comparison with AS computations in Fig. A1, this model seems irrelevant since a dislocation crossing several Peierls valleys yields to $\tau_c \to 0$ as $L_y \to \infty$.
Model C: The effect of τ_p on the dislocation shape is tentatively taken into account by subtracting τ_p^{eff} to τ_c in Eq. 2. Despite this crude assumption of a constant effective Peierls stress along the dislocation, it is clear from Fig. A1 that the computation of τ_c through the model C provides a satisfactory estimate in comparison with the AS results. We emphasize that no adjustable parameters are introduced in the final form of τ_c since τ_p, ϕ and f_m have been computed from independent simulations.

The importance of this correction increases as the crystal Peierls stress. It thus remains small for the edge dislocation. On the other hand, the same approach could present some interest in body-centered cubic alloy for which the screw Peierls stress can be much larger than in fcc alloys.

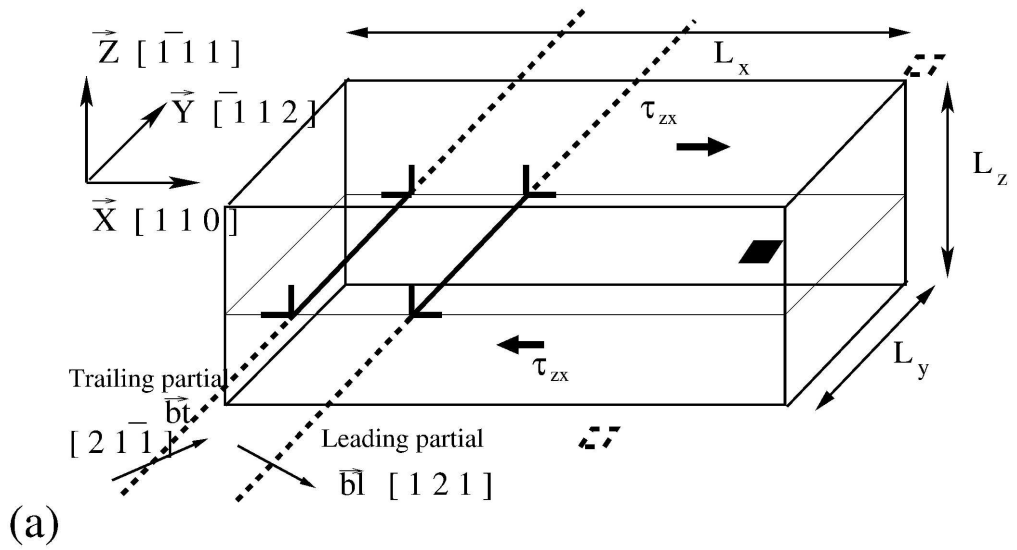

Schematic view of the simulation cell with a dissociated edge dislocation (a) and a screw one (b). The dislocations interact with Mg obstacles (squares) forming with the periodic images a regularly spaced chain of obstacles.
264x144mm (600 x 600 DPI)

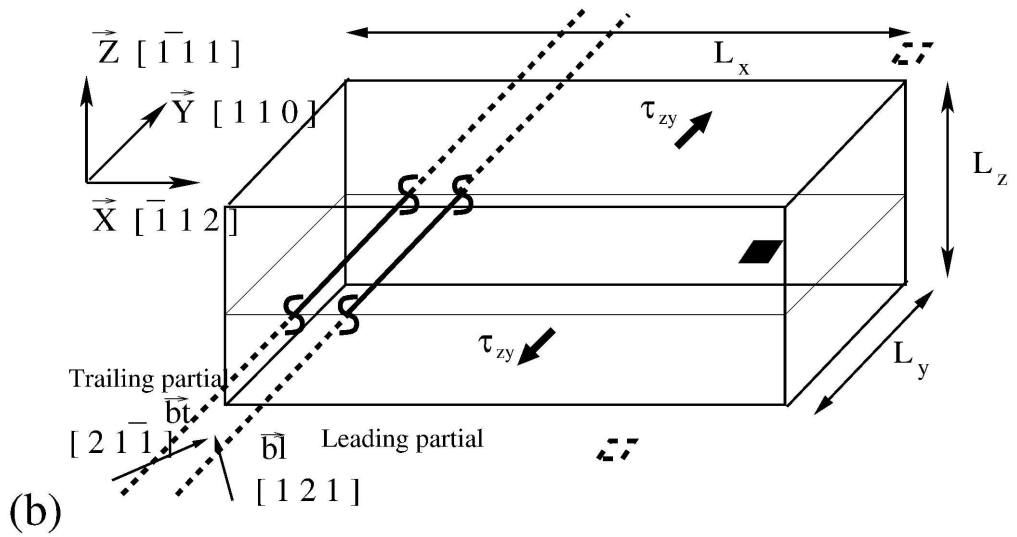

264x141mm (600 x 600 DPI)

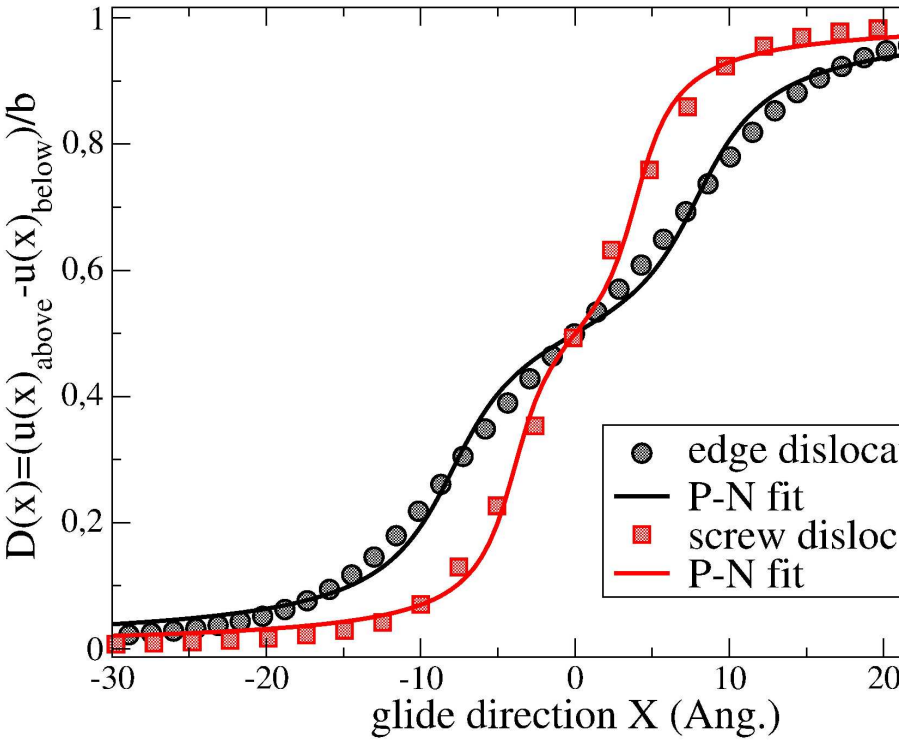

Normalized disregistry function D (see text) for the dislocation cores projected on the slip plane in the glide direction, X, for an edge (circle) and a screw (square) dislocation. The symbols correspond to atomic calculations while the lines are the results of the adjustment of the Peierls-Nabarro equation 1.
215x279mm (600 x 600 DPI)

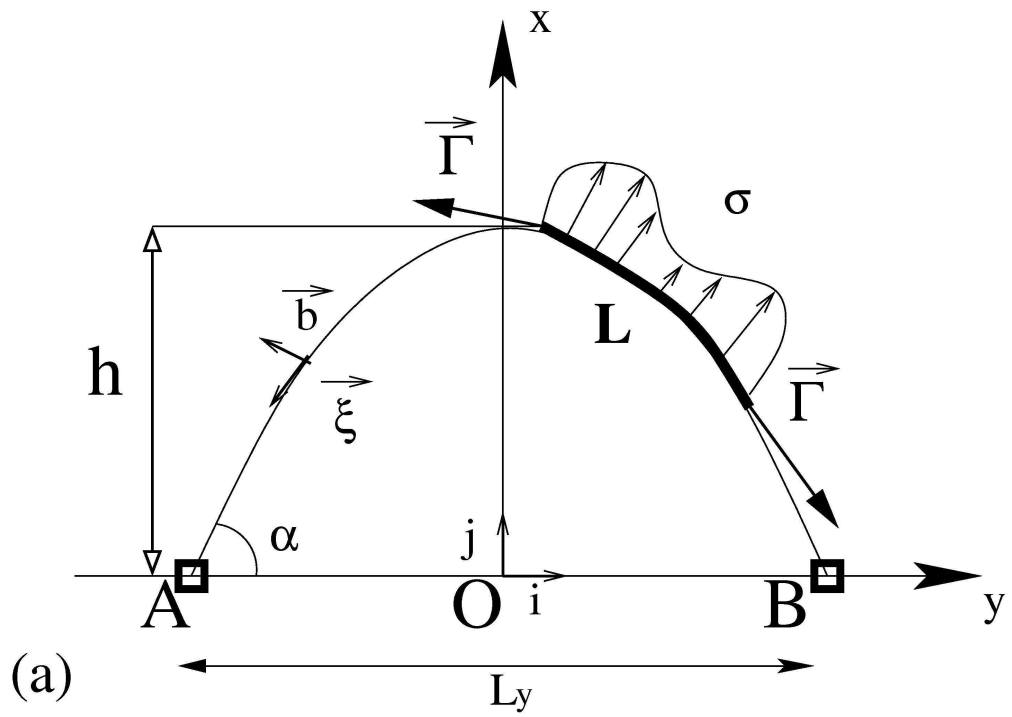

Schematic view of the forces acting on a bowed-out dislocation between pinning centers.
122x87mm (600 x 600 DPI)

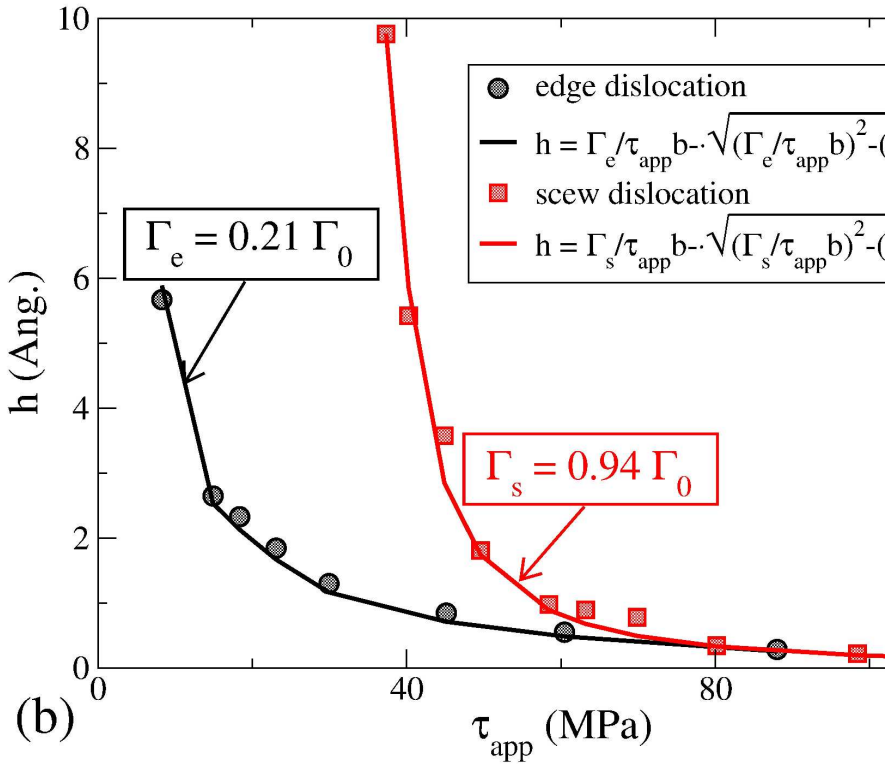

Amplitude of bowing-out h for the pinned dislocation against the external applied stress $\tau_{\textrm app}$, for different dislocation lengths, Ly. The circle (square) symbols correspond to the simulated edge (screw) dislocation while the lines are the adjustments of the line tension relation given in equation 5.
215x279mm (600 x 600 DPI)

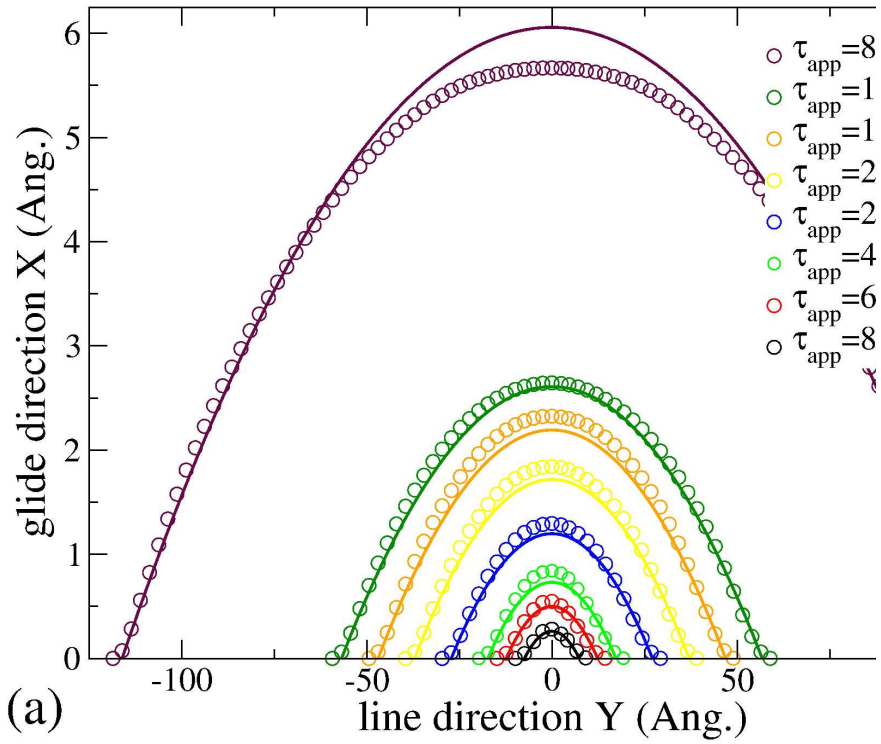

Comparison of the bow-out obtained by atomic-scale calculation (symbols) and line tension approximation (lines) given by Eq. 6 for edge (a) and screw (b) dislocations.
215x279mm (600 x 600 DPI)

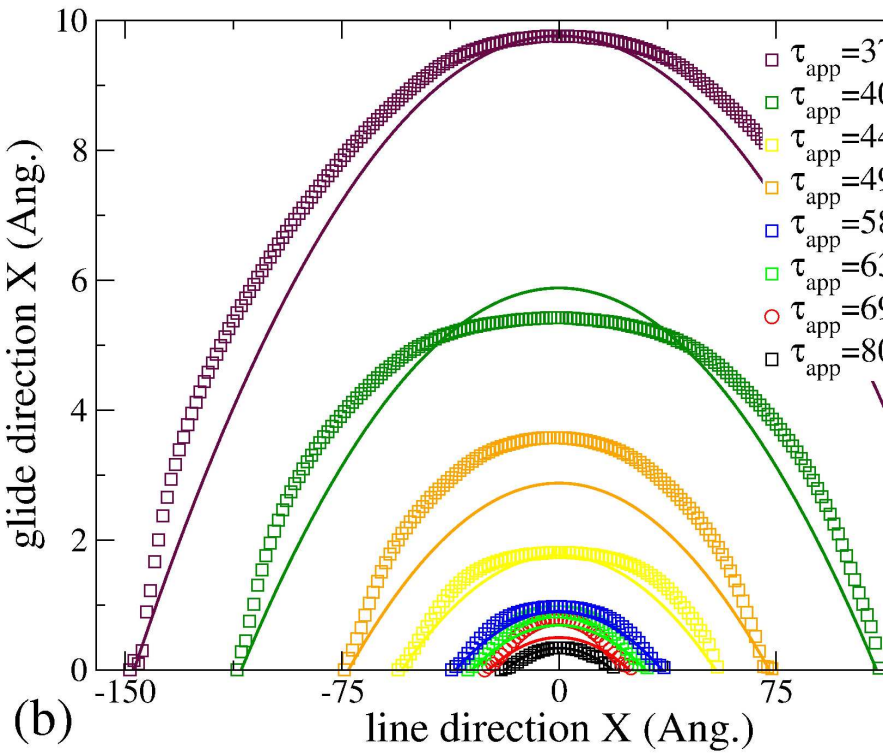

215x279mm (600 x 600 DPI)

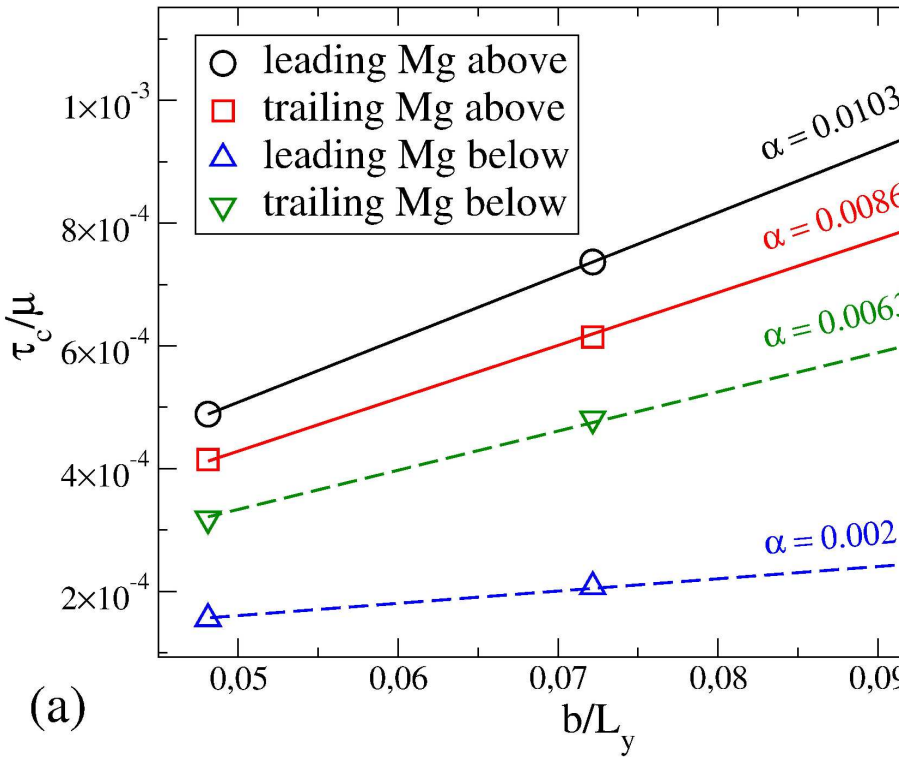

The normalized critical stress versus the normalized inverse distance between pinning centers along the dislocation line for Mg atom situated in the vicinity of the glide plane, and for edge (a) and screw (b) dislocations. According to Eq. 8, the linear interpolations of the critical stress associated with the leading and trailing partials are represented as continuous lines for the obstacle situated in the plane just above the glide plane whereas dashed lines correspond to Mg in the plane just below the glide plane.
215x279mm (600 x 600 DPI)

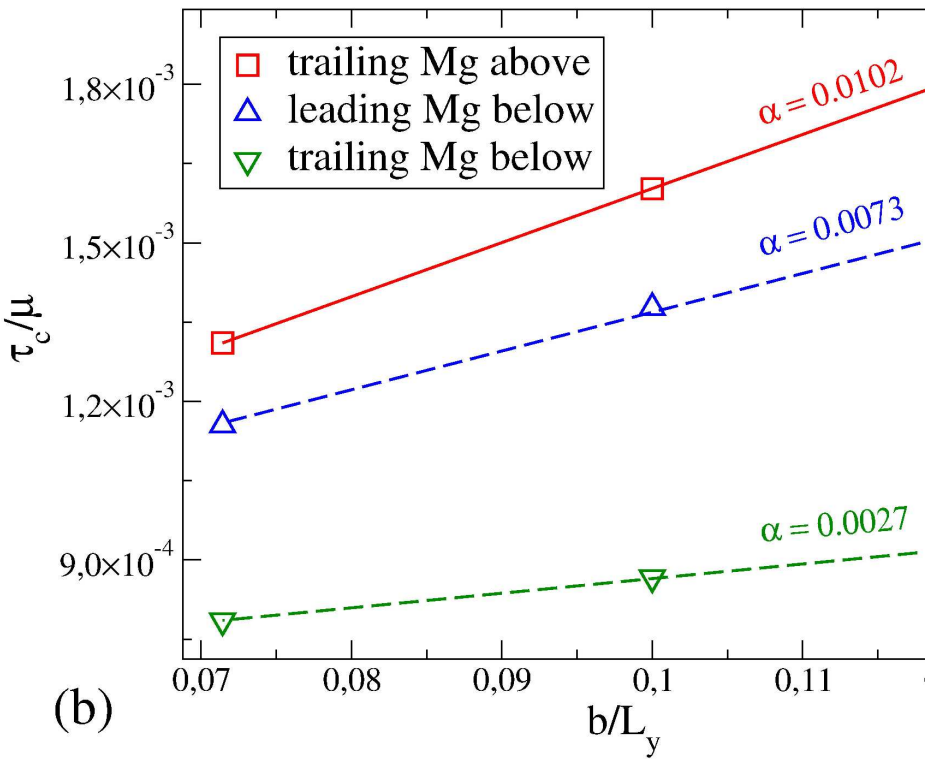

215x279mm (600 x 600 DPI)

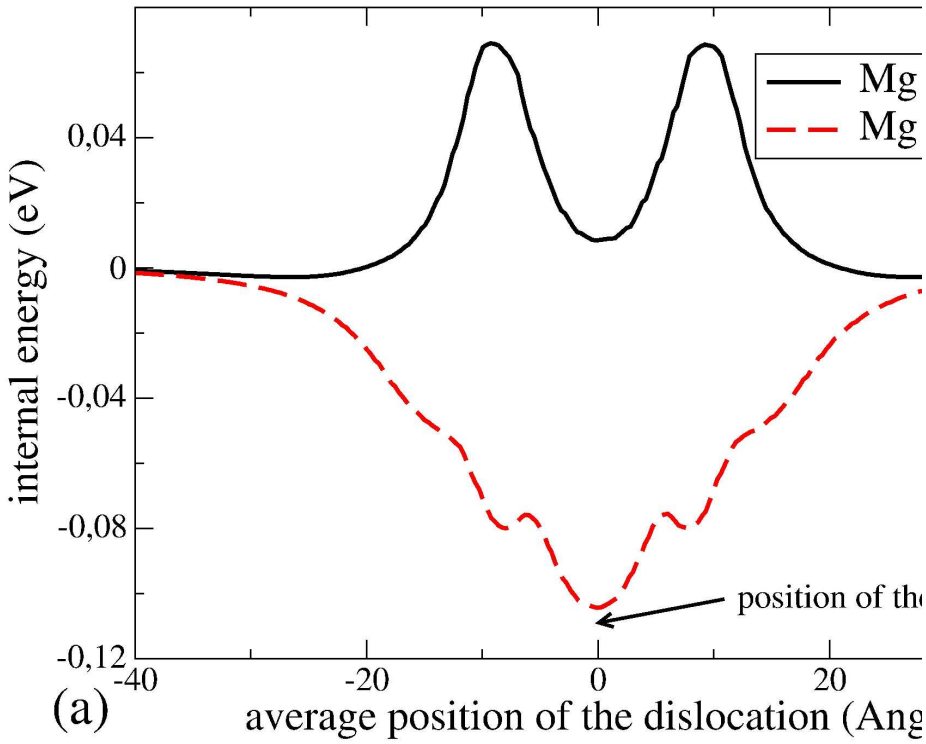

Internal energy of the simulation box versus the average position of the edge (a) and the screw (b) dislocation core. The simulation box contains a single obstacle formed by one isolated Mg solute atom situated either in the plane above the glide plane (full line) or the plane below the glide plane (dashed line).
215x279mm (600 x 600 DPI)

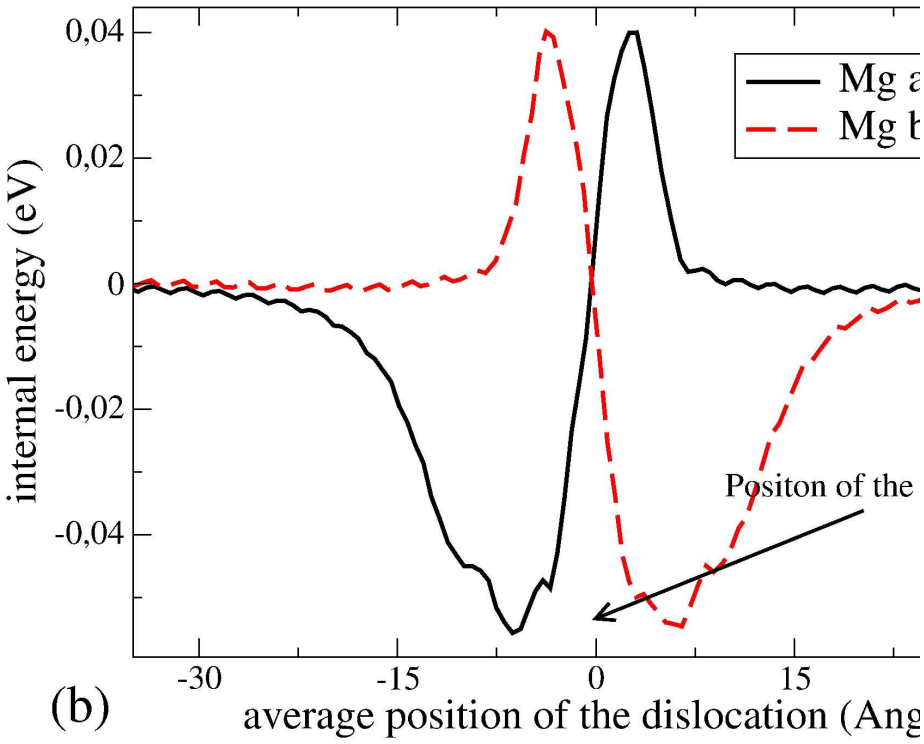

215x279mm (600 x 600 DPI)

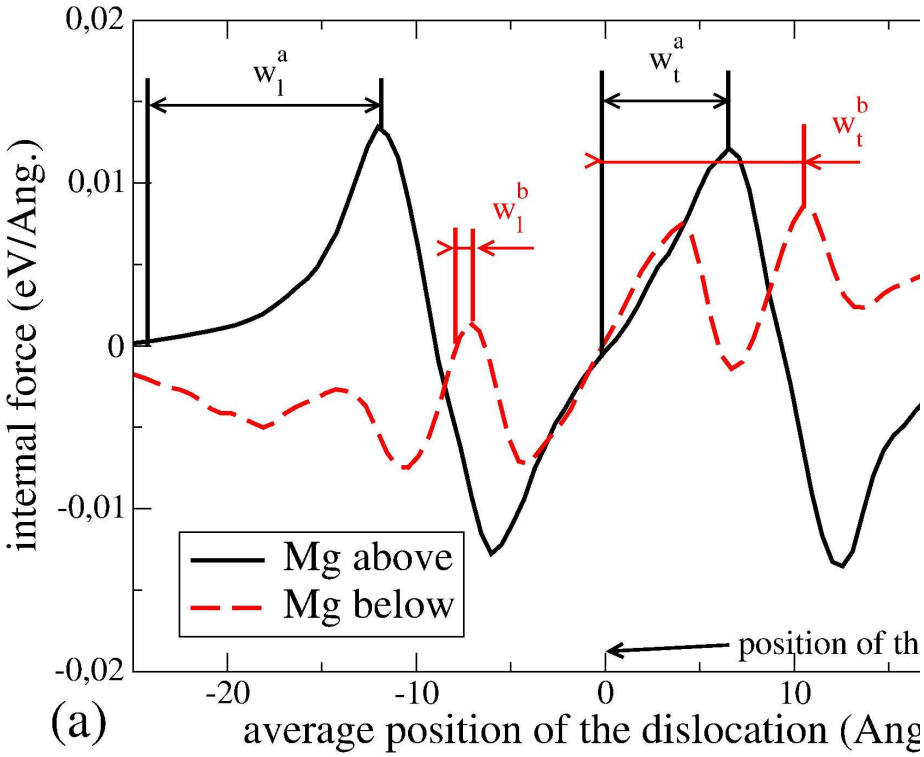

Internal force versus dislocation average position: the derivative of the internal energy of figure 6 for an edge (a) and a screw (b) dislocation. The full and dashed lines correspond to obstacles formed by one isolated Mg solute atom situated in the plane above (see w(a) in Tab.1) and below (see w(b) in Tab. 1) the glide plane, respectively.
215x279mm (600 x 600 DPI)

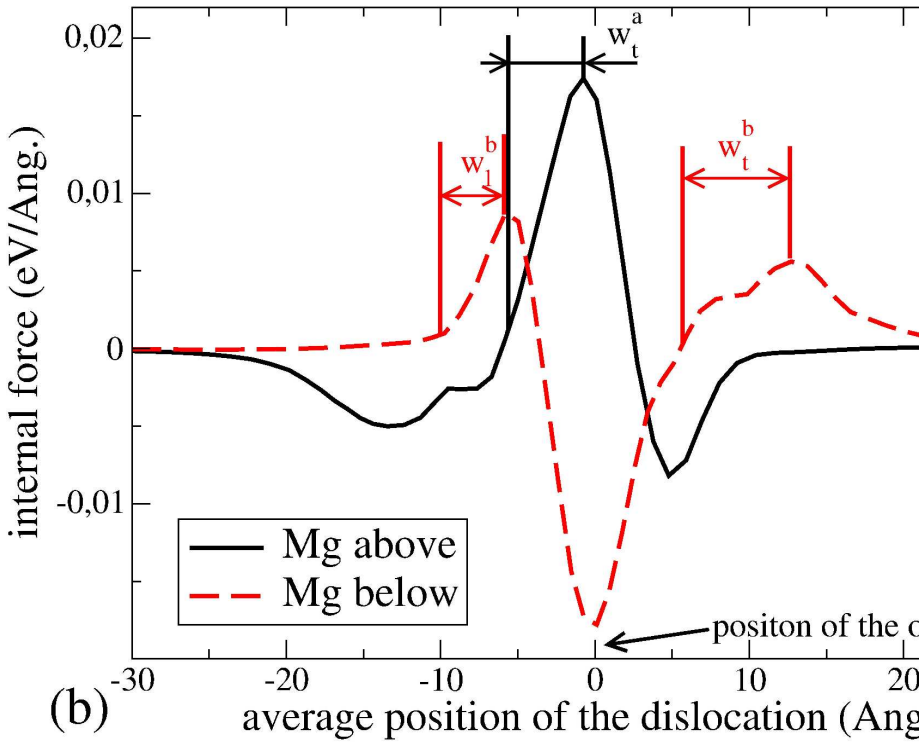

215x279mm (600 x 600 DPI)

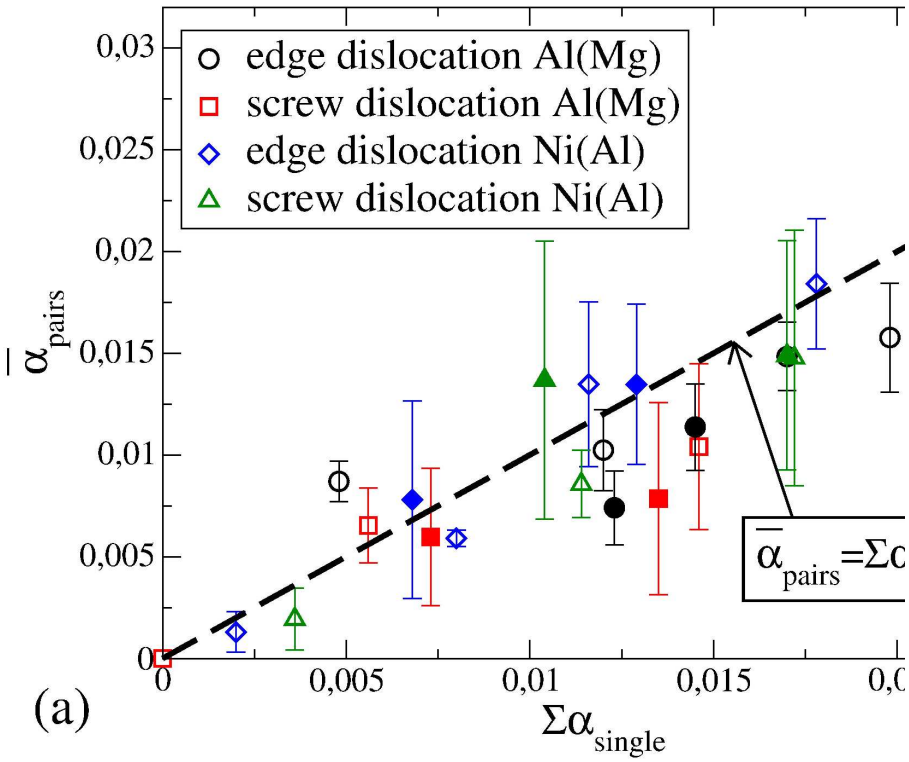

Average pinning coefficient of solute dimers as a function of the linear combination of the pinning strength of two isolated solutes which the superimposition corresponds to the dimer. The solute dimers that cross the slip plane are represented by full symbols while open symbols are used for those that do not cross the slip plane.
215x279mm (600 x 600 DPI)

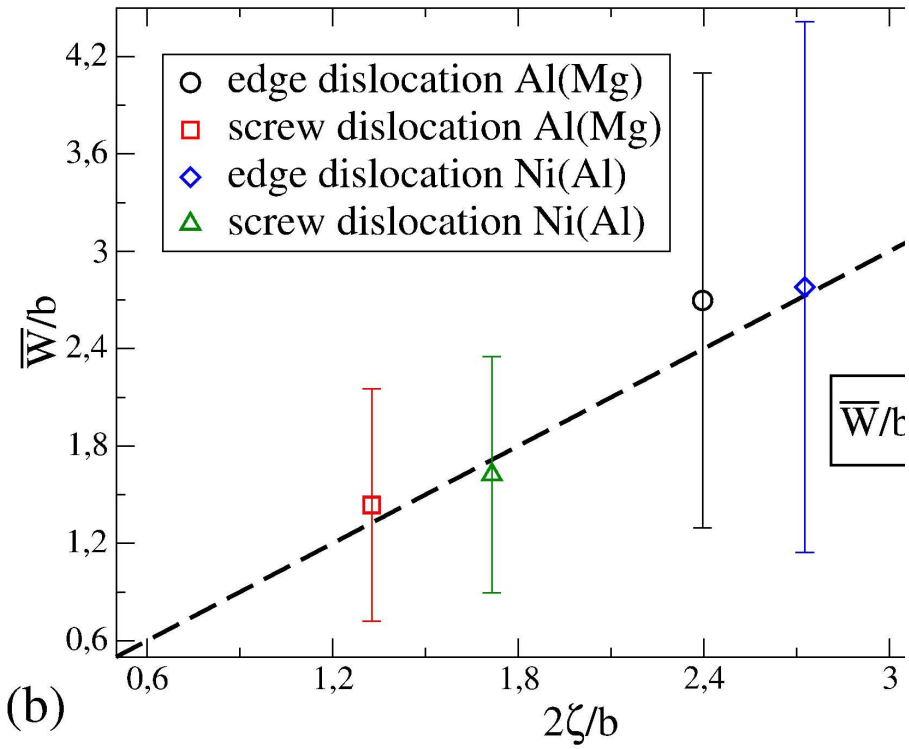

Normalized interaction range averaged over all the obstacle geometries against the normalized dislocation core widths for both dislocation segments edge and screw. The results for two different fcc alloys are presented: Mg solutes in Al (present work) and Al solutes in Ni from Ref. [18, 35]
215x279mm (600 x 600 DPI)

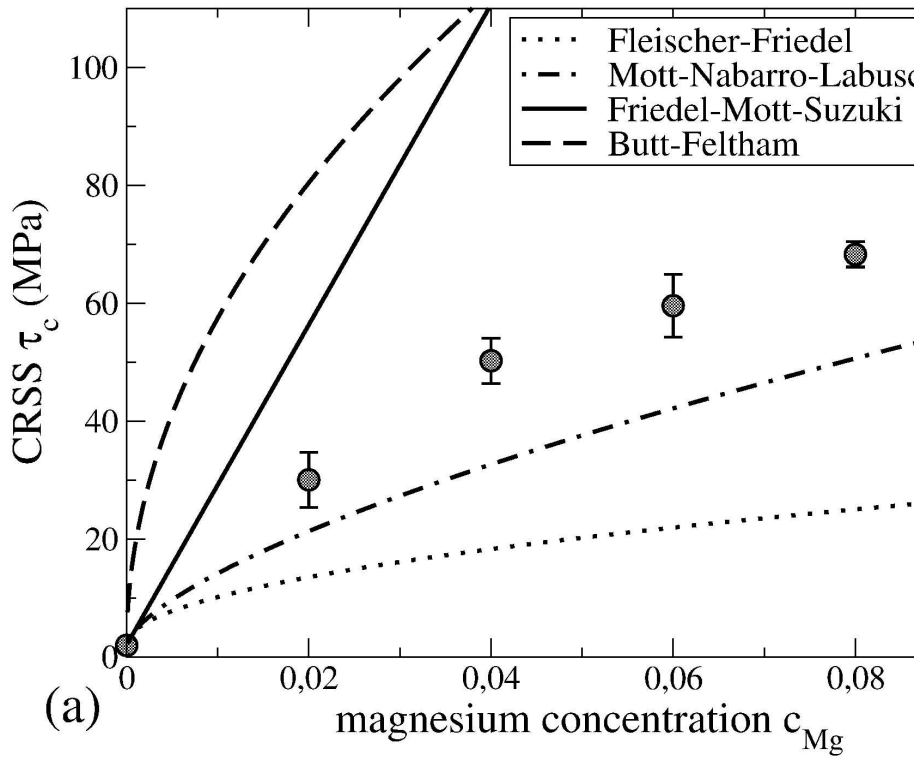

Variation of the critical resolved shear stress (CRSS) for an edge dislocation (a) and for a screw dislocation (b) against the Mg concentration, cMg, computed from the atomic-scale simulations (AS) with different Mg random distributions (symbols). The estimations made from the analytical models (see Tab. 2) have also been reported: Fleischer-Friedel (dotted line), Mott-Nabarro-Labusch (dot-dashed line), Friedel-Mott-Suzuki (full line) and Butt-Feltham (dashed line).
215x279mm (600 x 600 DPI)

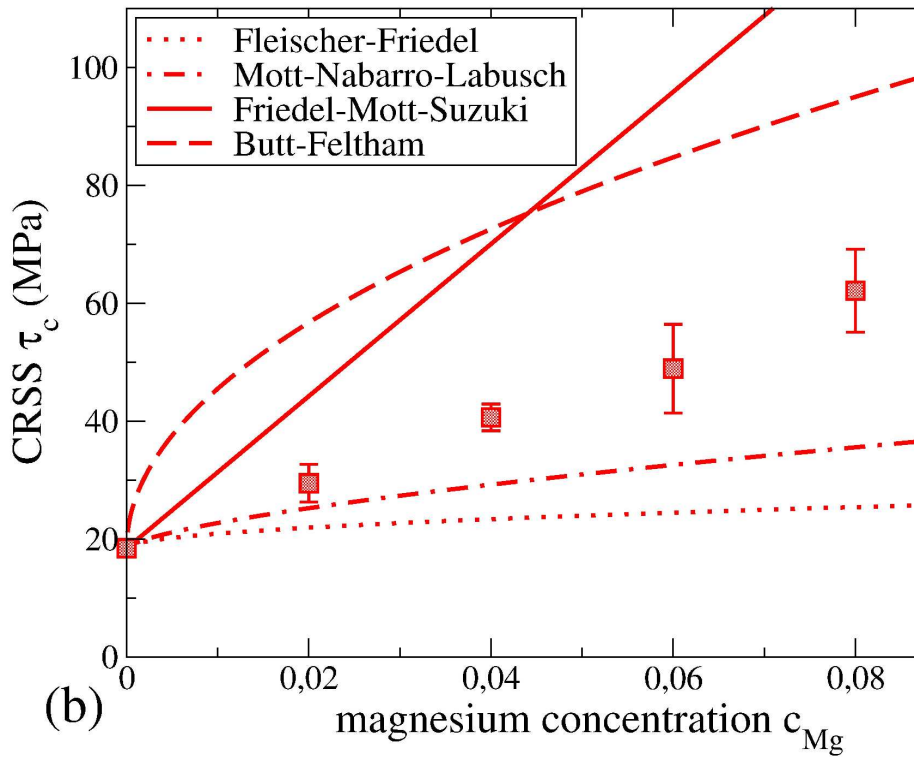

215x279mm (600 x 600 DPI)

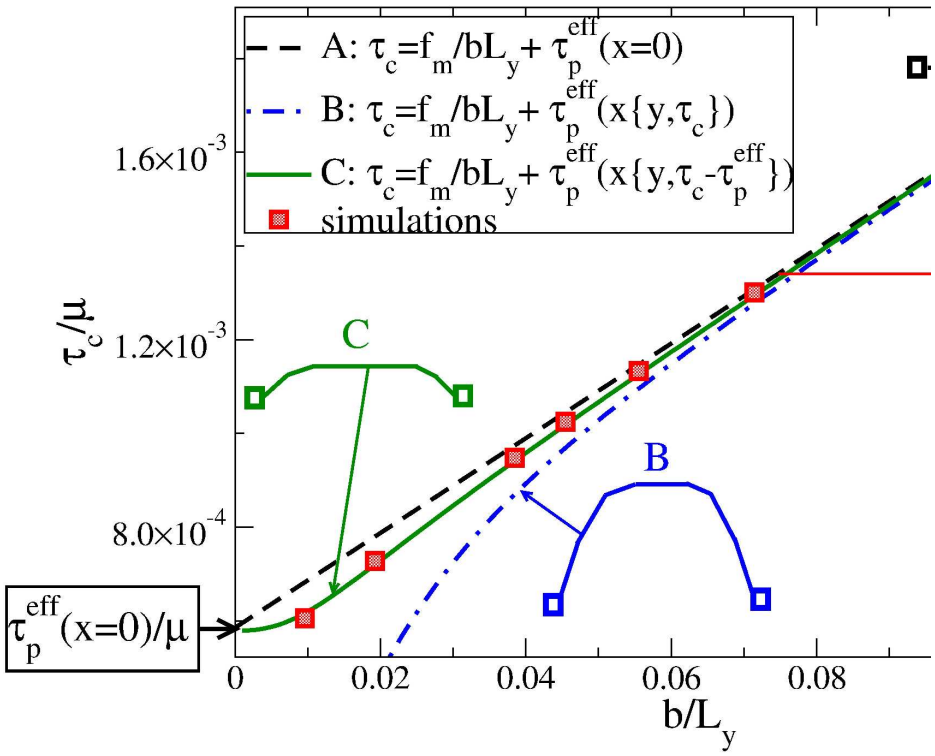

Normalized critical stress (square) that needs a screw dislocation to overcome an isolated Mg solute atom situated in the plane just above the glide plane versus the normalized inverse distance between pinning centers along the dislocation line. The critical stresses are computed under various assumptions regarding dislocation pinned shapes. A: flat dislocation (dashed line), B: large bending (dot-dashed line) and C: small bending (continuous line) accounting for the effective Peierls stress.
215x279mm (600 x 600 DPI)